Optoelectronic Integration Using the Magnetically Assisted Statistical Assembly Technique: Initial Magnetic Characterization and Process Development

by

Joseph John Rumpler II

Submitted to the Department of Electrical Engineering and Computer Science
in partial fulfillment of the requirements for the degree of

Master of Science in Electrical Engineering

at the

Massachusetts Institute of Technology

September 2002

Author.....
Department of Electrical Engineering and Computer Science
September 5, 2002

Certified by.....
Clifton G. Fonstad, Jr.
Professor of Electrical Engineering
Thesis Supervisor

Accepted by.....
Arthur C. Smith
Chairman, Department Committee on Graduate Students

Optoelectronic Integration Using the Magnetically Assisted Statistical Assembly Technique:
Initial Magnetic Characterization and Process Development

by

Joseph John Rumpler II

Submitted to the Department of Electrical Engineering and Computer Science
on September 5, 2002 in partial fulfillment of the
requirements for the degree of
Master of Science in Electrical Engineering

Abstract

The commercial integration of optoelectronic devices heavily relies on hybrid techniques such as wire bonding and flip-chip bonding. These methods are limited in the scale and flexibility in integration. Research focused on optoelectronic integration is performed using numerous techniques such as direct epitaxy, full-scale wafer bonding, and self-assembly. Magnetically Assisted Statistical Assembly (MASA) is an example of the latter technique and improves scale and flexibility by enabling the simultaneous integration of large numbers of individual devices. This thesis work is focused on the demonstration of the MASA concept through characterization of the magnetic materials forming the foundation for this technique and development of an adequate process technology. Both, the magnetic characteristics and the process technology required to integrate the technology are presented along with results of the integration.

Thesis Supervisor: Clifton G. Fonstad Jr.
Title: Professor of Electrical Engineering

Acknowledgements

A debt of gratitude is owed to a number of individuals who have helped me beyond measure the last two years. First, let me thank Professor Clif Fonstad who envisioned the Magnetically Assisted Statistical Assembly (MASA) technique and who has provided tremendous support and guidance on the project.

To the members of Professor Fonstad's group, I give my sincere thanks. Especially to James Perkins who has been there every step of the way developing the MASA process with me. The collaboration has been a very productive and enjoyable experience. To Eralp, my officemate, with whom I have had many dinner conversations on optoelectronic communications the past couple of years. To Henry Choy and Wojciech Giziewicz, for answering countless processing questions and for giving me a wealth of helpful new graduate student advice. To Ed Barkley for listening to me give updates on the MASA pill making business and for creating a dynamite exercise routine that helps rejuvenate me after long hours in the fab. To Mike Masaki for his advice on classes and helping me adjust to graduate school. To Prof. Sheila Prasad for always providing a friendly face around the third floor of Building 13.

Thanks to Kurt Broderick who has been very accessible in terms of training and fixing equipment in EML. In the CMSE, thanks go to Libby Shaw for her accessibility for training on the magnetic force microscope and to Tim McClure for training on the profilometer.

Thanks to Dr. Bob O'Handley for insightful discussions on magnetics as well as for the use of his vibrating sample magnetometer and torque magnetometer.

I'd like to thank my family who have been there for me every step of the way. To my parents, Joe and JoAnn, who listen to me ramble on and on about the trials and tribulations of a graduate student and who are always interested in what's going on in my life. The support I have received from you for these past 26 years has been tremendous and words

cannot describe my appreciation. To my brothers Jim and Jason who provide me with some needed diversions. To my sisters Jan and Jill and their families for their interest in what I am doing.

I would like to dedicate this thesis to my grandmother Dolores Greiwe who passed away this August and who was a very special person in my family.

Contents

List of Figures

List of Tables

Chapter 1

Modern Optoelectronic Integration

1.1 Motivation for Optoelectronic Integration

Commercial optoelectronic devices define the communications industry where the high transmission bandwidth characteristic of optical signals and the information processing capability of electronic circuits are combined. For instance, high-speed optoelectronic transceivers transmit and receive optical signals, optical modulators use an electrical signal to encode a signal optically, and optical waveguides with integrated photodetectors monitor signals traveling through the communications network. In addition, optoelectronic devices are essential in other product areas such as visual display technology and sensing applications.

In modern optoelectronic devices, the required electronics must satisfy two basic needs, low power consumption and high frequency performance. Depending on the application, the relative importance of these variables will vary. For instance, very high frequency electronics are needed for dynamic applications such as clock recovery circuits following the photodetector in an optical receiver. Gallium arsenide (GaAs) based and indium phosphide (InP) based heterojunction bipolar transistors (HBT) and high electron mobility transistors (HEMT) as well as silicon germanium (SiGe) bipolar transistors are typically used for these applications due to their high cutoff frequencies (Figure 1-1).

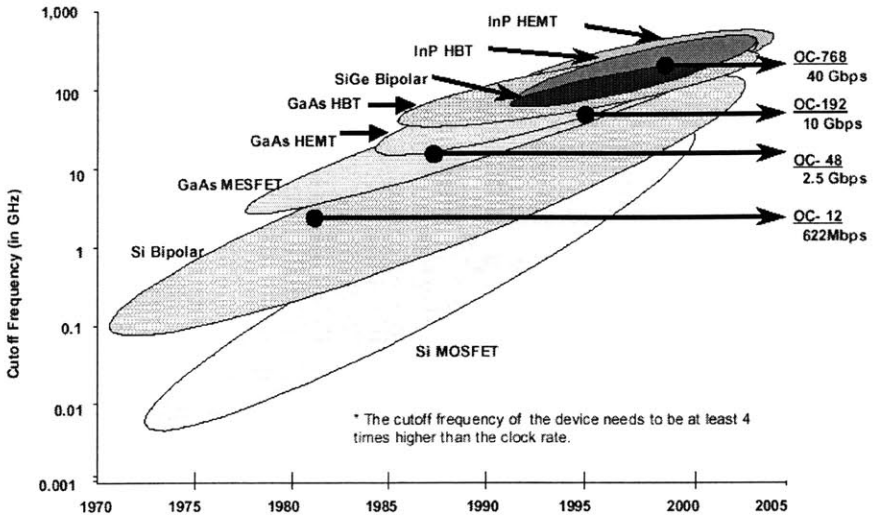

Figure 1-1: Cutoff frequency as a function of material system and transistor type over the past thirty years [1].

Low static power consumption electronics are also needed for applications such as memory where most transistors remain in a certain state for an extended period of time. Silicon complementary metal oxide semiconductor (CMOS) technology is used in memory applications due to the fact that it operates with no static power dissipation. Thus, if a CMOS circuit is not being switched from on to off or vice versa, a CMOS circuit will not dissipate power. By keeping the static power to a minimum, it is possible to prevent the circuit from overheating. Unfortunately, CMOS technology cannot be implemented in other materials such as InP or GaAs because of the inability to form the high quality, low-defect oxide required for CMOS.

Similarly, depending on which optoelectronic circuit is being designed, the necessary characteristics of optical emitters and detectors will differ. A main requirement for these devices is the wavelength of light that they emit or detect. Figure 1-2 shows the materials most commonly used to manufacture emitters that cover a wide range of wavelengths. Figure 1-3 displays two important figures of merit for photodetectors, quantum efficiency and responsivity, as a function of material and wavelength.

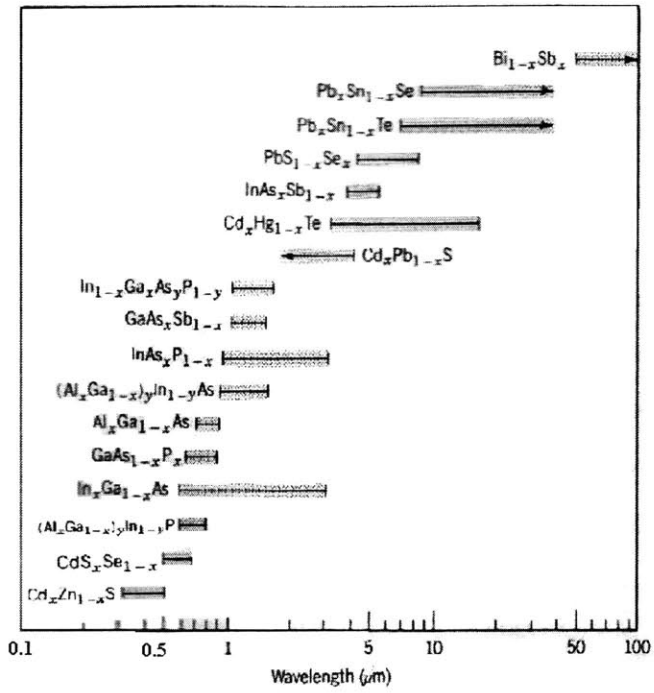

Figure 1-2: Optimum laser materials as a function of emission wavelength [2].

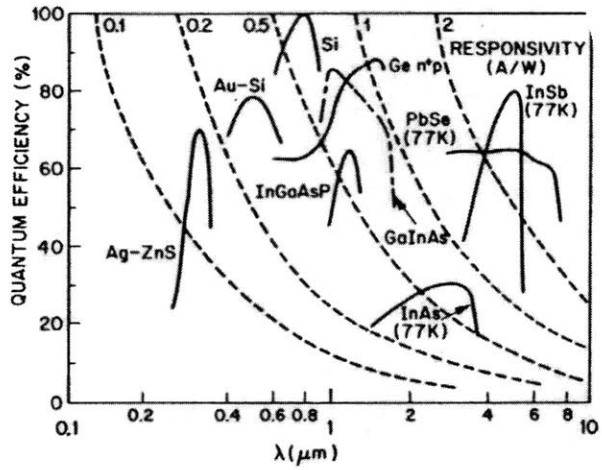

Figure 1-3: Photodetector quantum efficiency and responsivity as a function of material [3].

Taking the integration of optical emitters with memory intensive electronic circuits, as an example, monolithic optoelectronic integration has proven difficult for multiple reasons. First, the material typically used for memory intensive electronic circuits, silicon, is a poor light emitter due to its indirect energy bandgap. Direct energy bandgap III-V compound semiconductor materials such as InP and GaAs have much better optical emission properties and thus are used to produce lasers and light emitting diodes (LED). However, the memory intensive electronics associated with these III-V materials is inferior to silicon because of the inability to implement CMOS technology.

Regarding the integration of high-speed dynamic circuits with optical emitters as is the case for a high-speed transmitter with a driver application specific integrated circuit (ASIC), the integration has proven difficult for another reason. Both high quality optical emitters at appropriate wavelengths and output powers and as well as very high quality

high frequency circuits can be made using III-V semiconductors. In spite of this, the processing constraints of optical devices typically do not correspond well with the constraints of standard electronics processes. For instance, optical devices are usually very thick devices; whereas, electronics are typically very thin. Thus, photolithographic patterning of topographic features is very problematic. In addition, fabricating optical devices such as vertical cavity surface emitting lasers (VCSEL) alongside electronics limits the processing temperatures that can be achieved and thus limits the quality of the devices.

Therefore, the major issues concerning optoelectronic integration that have prevented true monolithic integration are twofold. First, for many applications different materials systems are required to manufacture the devices involved in the integration. Materials issues have prevented the combination of these materials yielding functional devices. Second, when the devices to be integrated are from the same material system, the fabrication processes mandated by the devices are usually incompatible.

1.2 Commercial Approaches

Because of the problems associated with fabricating monolithic optoelectronic devices, the commercial manufacture of these devices typically involves a hybrid technique where heterogeneous devices are optimally processed separately prior to integration. Then integration consists of either wire bonding or flip-chip bonding.

Wire bonding as its name implies involves the soldering of fine wires between contact pads. As higher density integrations of high data rate devices are implemented, wire parasitics that degrade the signal and the time required to perform the wire bond make this technique prohibitive.

Flip-chip bonding involves the deposition of solder bumps on a substrate and the alignment of a die to the substrate. Once aligned, pressure is applied and the temperature is increased in order to aid the bonding. An underfill is often deposited between the die

and the substrate to reduce the stress resulting from the thermal expansion coefficient mismatch of the materials being integrated.

Flip-chip bonding offers markedly better performance with regards to assembly time and parasitics than wire bonding. Thus, for high frequency applications, flip-chip is the standard integration technology used in the optoelectronics industry. The issue with flip-chip bonding is that the largest die size that can be reliably bonded is about 1 cm^2. This upper limit arises since as the bonded die size increases, the temperature and time required for bonding increase as well. Exposed to high temperatures, the underfill between the die and the substrate undergoes significant stresses. In addition, the larger the size of the die being bonded, the more difficult it is to flow the underfill between the die and substrate without encountering air bubbles. For the communications industry where reliability standards are stringent, flip-chip bonding is an imperfect solution [4].

Flip-chip is an acceptable solution at the moment since integration has primarily involved only small numbers of light sources and detectors with associated controlling electronics for systems operating at low data rates. If one is to implement truly optoelectronic large-scale integration for high bandwidth systems, then a technique offering less assembly time with less parasitics must be developed. Furthermore, it would be ideal to have a technology where further processing could be undertaken after the devices have been integrated.

1.3 Research Approaches

The integration of compound semiconductors with silicon has been investigated for over two decades. For large-scale optoelectronic integration, the two techniques that have garnered considerable attention during this time period are direct epitaxy and wafer bonding. An improvement over the scale of wire bonding and flip-chip bonding, these methods attempt to integrate entire wafers of devices at once. Most recently, techniques involving fluidic assembly have gained popularity in the research community.

1.3.1 Direct Epitaxy

Direct epitaxy has been investigated for optoelectronic integration with the goal that one day it could allow for a truly monolithic process. Using the integration of Si and GaAs as a reference, direct epitaxy is typically carried out by epitaxially growing a thick layer of GaAs on Si. By growing a thick layer, the goal is to enable the lattice deep inside the GaAs to relax from its strained state at the GaAs/Si interface that results from the 4% lattice constant mismatch. Unfortunately, if the devices are functional after processing, their lifetimes prove to be very short. These device failures are a result of both the stress due to the lattice mismatch and the stress related to the mismatch of the materials' thermal expansion coefficients (CTE). Since GaAs has a CTE almost three times that of Si, the elevated temperature of the growth process often results in catastrophic stress related defects [5].

Parameter	Si	Ge	GaAs	InP
lattice constant (Å)	5.43095	5.64613	5.6533	5.8686
CTE (x 10^{-6} °C^{-1})	2.6	5.9	6.86	4.75

Table 1.1 Material parameters of Si, Ge, GaAs, and InP [5, 6].

To alleviate the problems with the lattice mismatch, some research groups are trying to buffer the interface between Si and GaAs with intermediate lattice constant material. One approach uses SiGe buffer layers to achieve three orders of magnitude reduction in the dislocation density from 10^9 cm^{-2} to 10^6 cm^{-2} from the direct epitaxy of GaAs on Si [7]. Typically, the process begins by growing layers of SiGe having a high Si content on a Si substrate. As more and more layers are grown, the content of the layers are given higher and higher Ge content. Finally, the GaAs layer is grown. Another approach developed by Motorola, utilizes a strontium titanate layer to mitigate the lattice constant mismatch [8]. At this time, no specific details have been released to explain this technology and demonstrate that it in fact has potential for commercial use.

1.3.2 Wafer Bonding

Wafer bonding improves upon direct epitaxy by allowing for the optimum processing of devices prior to integration. Furthermore, wafer bonding removes the strain due to the lattice constant mismatch. However, the CTE mismatch remains a difficult obstacle to overcome [5].

The typical wafer bonding process involves the bringing together of a semiconductor-to-semiconductor interface or a semiconductor-to-insulator interface. This differs from flip-chip bonding where a metal-to-metal contact is achieved. A typical bonding process begins with the planarization of the two wafers to be bonded. Then, the wafers are brought in intimate contact. Next, the temperature is raised slightly to aid in the bond formation. The maximum bonding temperature is limited by the CTE mismatch between the two wafers. Typically, the backside surface of one of the wafers is then thinned to allow for the straightforward formation of interconnect vias and interconnections to the devices.

The major issue with wafer bonding is the stress that the wafers undergo which can prove fatal for the devices. The stress problem is magnified since the devices are all linked together and thus the stresses couple along the entire wafer.

Bonding techniques such as Aligned Pillar Bonding (APB) have been developed that lessen the problem of the CTE mismatch. In APB, Si devices and GaAs devices are optimally processed separately. Then, GaAs device pillars on the order of tens of microns diameter on the device wafer and correspondingly sized recesses on a host Si wafer are patterned. The wafers are next aligned and bonded. The GaAs substrate is removed and thus the decoupling of the devices has been implemented. Issues with APB are the fact that it sacrifices much semiconductor material and it is difficult to align the wafers [5].

1.3.3 Fluidic Assembly Techniques

Given the stress issues involved with wafer bonding and direct epitaxy, research is being performed involving the parallel integration of uncoupled pre-processed devices in aqueous solutions. Like wafer bonding, these techniques involve the optimum processing of devices on their own device specific wafer prior to integration. In the fluidic assembly technique's most basic form, one wafer will have large numbers of unconnected devices and the other target wafer will have interconnected components and recesses with dimensions corresponding to the devices on the device wafer. Improving on wafer bonding, the devices on the former wafer are etched free from their substrate, thus decoupling them from one another. The etched free devices are then drawn to the target wafer by some force mechanism. The two main techniques being investigated are Fluidic Self-Assembly and Electric Field Directed Assembly.

1.3.3.1 Fluidic Self-Assembly (FSA)

Fluidic Self-Assembly (FSA) utilizes the force of gravity to direct trapezoidal shaped devices to a target wafer having correspondingly shaped recesses. Patterning the devices with a particular shape ensures that the devices assemble with the proper orientation and removes the need for manual alignment. The trapezoidal shape was chosen for its horizontal symmetry in order to simplify alignment [9]. Once etched free from their sacrificial substrate, the devices are flowed over the target wafer in a fluid and self-assemble in the recesses. Once properly in the recess, a device remains there by a combination of Van der Waals forces and the force of gravity. After assembly, the wafer surface has a high degree of planarity thus facilitating the fabrication of device contacts [10].

1.3.3.2 Electric Field Directed Assembly

Whereas, FSA utilizes the force of gravity, Electric Field Directed Assembly (EFDA), as its name implies, uses electric fields to direct individual devices to a specific location on a target wafer. The principle by which this assembly technique operates is electrophoresis. Electrophoresis is the condition where attractive or repulsive forces act on particles due to an electric field. If a device is more polarizable than the dielectric medium in which it is contained, the device will be attracted in the direction of increasing electric field strength. By making use of this concept, devices can be placed at specific locations on a target substrate [11].

EFDA requires the fabrication of electrodes on the target wafer. When a voltage is applied to electrode present on the host substrate, an electrophoretic force is created that moves the device toward the biased electrode (Figure 1-4).

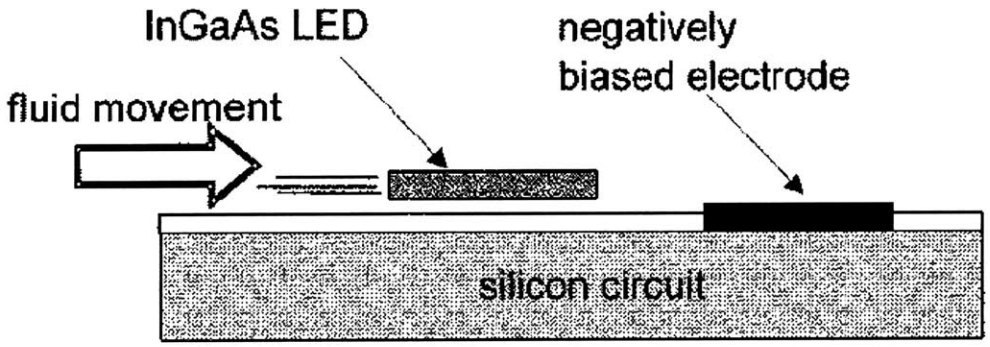

Figure 1-4: Electric Field Directed Assembly [12].

1.4 Thesis Organization

This work involves the demonstration of the Magnetically Assisted Statistical Assembly (MASA) Technique using gallium arsenide based heterostructures and a silicon substrate

with silicon dioxide recesses as the test vehicle. This technique offers a possible alternative to the two aforementioned fluidic assembly techniques, and this thesis is part of a larger effort to develop and evaluate MASA. Chapter 2 provides an overview of the MASA technology, implementation of the technology, and the magnetic requirements underlying the technology. Chapter 3 first includes a description of magnetic anisotropy and how it affects the attainable magnetic requirements mandated in Chapter 2. Chapter 3 also contains the characterization data on the magnetic materials used in the demonstration of MASA. Chapter 4 describes the fabrication steps required to implement the technology. Chapter 5 concludes the thesis and proposes future work that will be carried out.

1.5 Lab Facilities

Most of the fabrication described in this thesis was carried out in the Exploratory Materials Laboratory (EML), which is part of the Microsystems Technology Laboratories (MTL). The electrodeposition process, some of the wet chemical etching, and the final integration technique were carried out in Professor Fonstad's group laboratories. The Vibrating Sample Magnetometer and Torque Magnetometer characterization was carried out in the laboratory of Dr. R.C. O'Handley. The magnetic force microscope, atomic force microscope and profilometer characterization was carried out in the Shared Experimental Facilities (SEF), which is part of the Center for Materials Science and Engineering (CMSE).

Chapter 2

Magnetically Assisted Statistical Assembly (MASA)

2.1 Introduction to MASA

As the monolithic fabrication of optoelectronic devices and the bonding of entire wafers of devices have proven difficult, a research effort is now aimed at using fluidic assembly techniques to integrate individual heterogeneous devices in a large-scale manner. Magnetically Assisted Statistical Assembly (MASA) is a fluidic assembly technique that has many similarities with the Fluidic Self-Assembly and Electric Field Directed Assembly techniques described in Chapter 1. For instance, MASA, like the two aforementioned techniques involves the optimum processing of devices prior to integration. Second, the assembly occurs in an aqueous solution where the devices are allowed to freely fall under the force of gravity to the target substrate.

However, the mechanism in MASA by which a device is ultimately brought to the target substrate and retained there is novel. The MASA technique utilizes the inherent properties of ferromagnetic thin films to aid in the self-assembly and retention of heterogeneous devices.

The demonstration of the MASA technique involves the integration of cylindrical compound semiconductor heterostructure "pills" on a silicon host substrate. The pills are approximately 45 um in diameter and roughly 6 um thick. Correspondingly-sized silicon

dioxide recesses on the silicon host wafer are the targets for these pills. Magnetic films are deposited on both the pill and target substrates to provide the binding force that keeps the pills assembled in the recesses.

As is shown in Figure 2-1, the heterostructure pills are optimally processed on their own device specific substrate. A soft magnetic film is deposited on top of them. Then, these devices are patterned and etched free from the wafer and collected on an adhesive. The adhesive holding the pills is placed in a fluid whereby the adhesive dissolves and the pills remain in the solution.

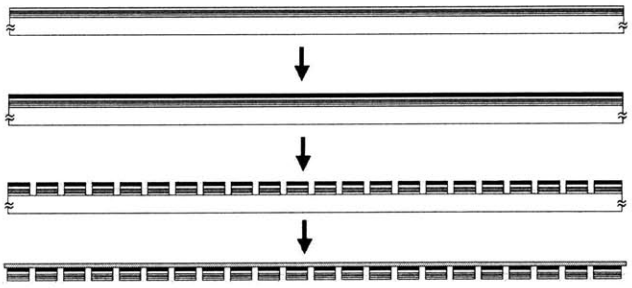

(a) Device heterostructure growth on bare semiconductor substrate.

(b) Soft magnetic layer deposition.

(c) Pill definition.

(d) Pill etch free and collection on adhesive.

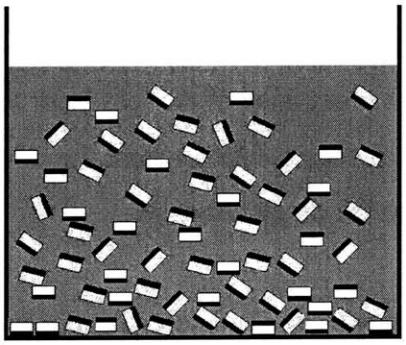

(e) Pills kept in solution.

Figure 2-1: Typical heterostructure pill process execution schematic.

As is shown in Figure 2-2, the host substrate process involves the deposition of a hard magnetic material. The hard magnetic film is patterned into a periodic pattern. Then, dielectric recesses having shape and size equivalent to the diode "pills" are formed on top of the hard magnetic layer.

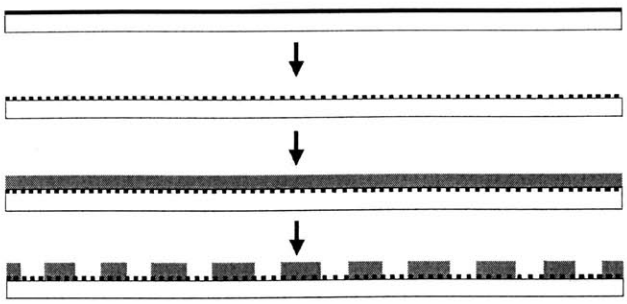

(a) Hard magnetic layer deposition on bare semiconductor substrate.

(b) Hard magnetic layer patterning.

(c) Dielectric deposition.

(d) Dielectric recess patterning.

Figure 2-2: Typical host substrate process execution schematic.

The assembly process, shown in Figure 2-3, consists of the flow of considerable numbers of heterostructure pills over the host substrate. As there are significantly more pills than host substrate recesses, it is probable that the dielectric recesses will be filled by the pills.

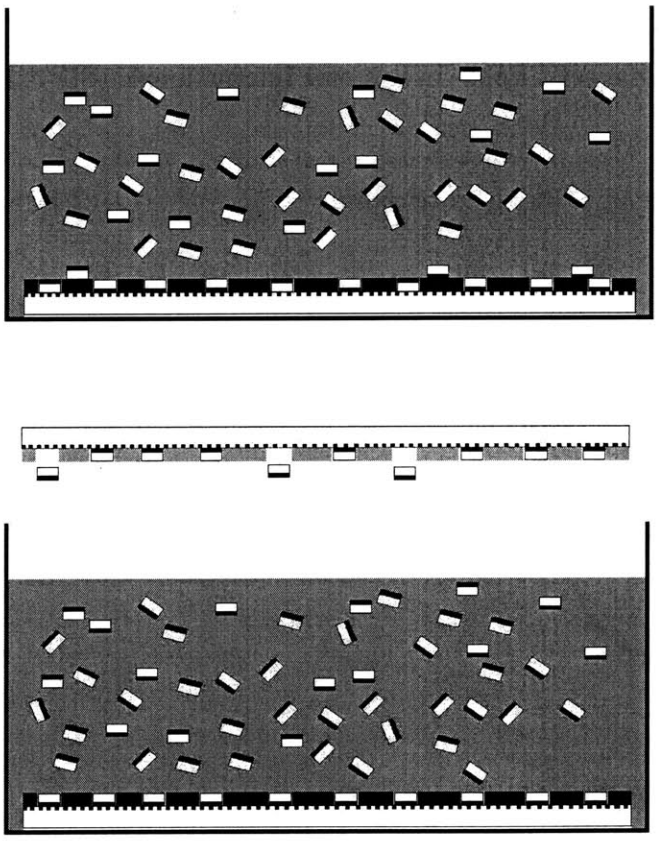

(a) Host wafer inundated with pills resulting in the assembly of pills in host wafer recesses.

(b) Host substrate flipped upside down to remove pills that have assembled incorrectly in recesses.

(c) After a few more trials, all pills assemble correctly in host wafer recesses.

Figure 2-3: MASA Assembly Process.

Once all the recesses are filled, the host substrate is flipped upside down. If the pills assembled right side up in the recesses, they will be retained on the host substrate by a significant magnetic force between the permanent magnet on the host substrate and the magnetically permeable film on the pills. If the pills assembled with the wrong side up, the force of gravity will cause the pills to be removed from the recesses. This process is repeated until all the recesses are properly filled.

2.2 Magnetic Properties Discussion

2.2.1 Hysteresis Loops

Before analyzing the aspects of the magnetic force binding the pills in the recesses, some basic properties of magnetic materials should be introduced. A magnetic material is characterized by its hysteresis loop (Figure 2-4). This is a plot of B, the magnetic flux density, as a function of H, the applied magnetic field. In Systeme Internationale (SI) units,

$$\vec{B} = \mu_O(\vec{H} + \vec{M}), \text{ where } \vec{M} \text{ is the magnetization.} \qquad (2.1)$$

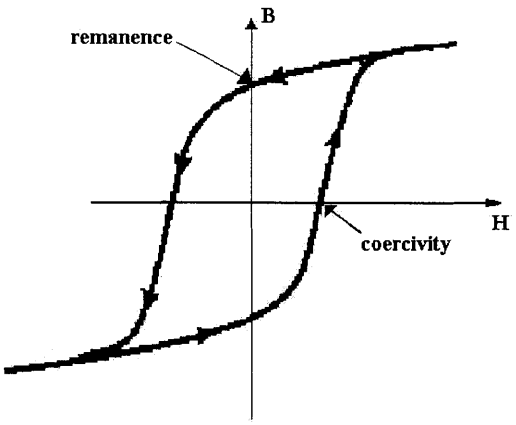

Figure 2-4: Typical magnetic hysteresis loop.

The main parameters that can be extrapolated from Figure 2-4 are the coercivity, H_c, the remanence, B_r, the saturation induction, B_s, and the permeability μ. The remanence, B_r is the flux density remaining when the external magnetic field, H, is reduced in magnitude to zero. The coercivity, H_c, is the magnetic field required to demagnetize the sample or in other words bring the magnetic flux density, B, to zero. The saturation induction, B_s, is the maximum value of magnetic flux density attainable in an external magnetic field. The saturation of the flux density, B, results from the saturation of the magnetization, M_s, and is related by the equation $\overrightarrow{B_s} = \mu_O(\vec{H} + \overrightarrow{M_s})$

The response of a material to an applied magnetic field is described by the magnetic permeability, μ. This quantity relates the magnetic field, H, and magnetic induction, B through the equation, $\mu = \frac{B}{H}$. Materials with high magnetic permeability produce a high magnetic induction when placed in a field H.

Properties such as the saturation magnetization, M_s, depend only on what material is used. For instance, all bulk nickel samples should have the same M_s. Properties such as coercivity, remanence, and permeability however depend on sample shape, stress, crystal structure, grain size, and other physical properties.

2.2.2 Hard and Soft Magnetic Materials

Magnetic materials can be classified as either being hard or soft (Figure 2-5). Hard magnetic materials typically have high coercivity and high remanence. These materials require larger applied magnetic fields to magnetize them than do soft magnetic materials. Moreover, once magnetized, hard magnetic materials are more difficult to demagnetize than soft magnetic materials. Therefore, hard magnetic materials are used to produce permanent magnets. Soft magnetic materials have lower remanence, lower coercivity, and higher permeability. These soft materials are relatively easy to magnetize and demagnetize.

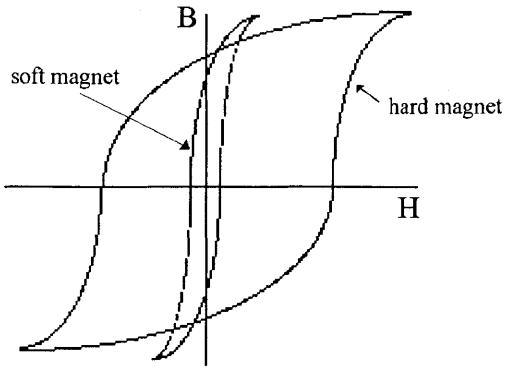

Figure 2-5: Hard and soft magnetic material hysteresis loops.

2.3 Magnetic Retentive Force

To ensure that the pills assemble properly in the recesses and to prevent the pills from inadvertently coming out of the recesses, magnetic films are used to generate a retentive force. This is the same force encountered when a big bulk permanent magnet attracts a magnetically permeable material. The only difference is that the magnets used in MASA have dimensions on the order of microns.

The main force that must be overcome for the pills to be retained is the force of gravity on the pills. The force per unit area due to gravity is on the order of 0.1 N/m^2 for typical pills studied here (Figure 2-6). If the retentive force is larger than the force of gravity acting on the pills, the pills should remain properly oriented in their recesses during wafer manipulation and transport

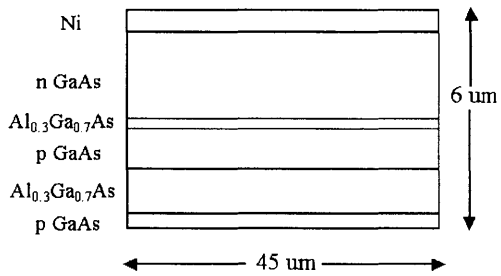

Figure 2-6: Heterostructure diode pill schematic.

To generate this sufficient retentive force, two magnetic films are needed. One layer is a hard magnetic film that acts as the permanent magnet in the assembly. The other layer is a soft magnetic film that can be easily magnetized by the hard magnetic film when the two films are in close proximity (< 1 um). One of these magnetic films is deposited on one side of the heterostructure pills and the other magnetic film is deposited on the host substrate. In this research effort, the hard magnetic layer was deposited on the host substrate and the soft magnetic layer was deposited on the pills.

2.3.1 Necessary Magnetic Criteria

For the retentive force to be sufficient, several criteria must be satisfied. First, since the assembly is performed with no external magnetic field applied, the hard magnetic layer must have a nonzero remanent magnetization, M_r, directed out of the plane of the film. Ideally a domain pattern shown in Figure 2-7 is achieved.

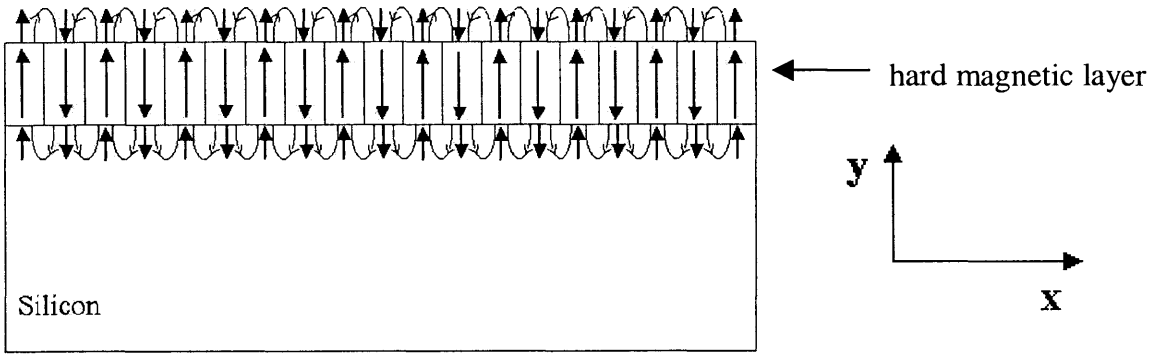

Figure 2-7: Theoretical magnetic domain pattern showing the corresponding external magnetic field of the hard magnetic film used in MASA.

With no applied magnetic field, the flux density generated by the hard magnetic film is $\vec{B} = \mu_O \overrightarrow{M_r}$. M_r should be significantly larger than the coercivity of the soft magnetic layer so that the hard magnetic layer can saturate the soft film and thus result in a

significant attractive force. Optimally, the hard magnetic layer M_r should be as large as possible.

Second, the hard magnetic layer should be sufficiently thick that the force due to the top surface of the magnetic film is significantly larger than the force due to the bottom surface. With a perpendicular-oriented material shown in Figure 2-7, the magnetic poles at the top surface of the film will be opposite the magnetic poles at the bottom surface of the film. Thus, the force due to the top surface will be directed anti-parallel to the force resulting from the bottom surface. The force on the pill will be stronger for whichever surface is closer to the pill. To obtain the largest total force, it is advantageous to have the film as thick as possible so that the force on the pill due to the top surface will greatly exceed the force due to the bottom surface.

Third, the hard magnetic layer should have a high coercivity, H_c, so as to prevent stray magnetic fields from demagnetizing the permanent magnetic layer. At a minimum, the hard magnetic layer coercivity should be larger than the soft magnetic material's remanent magnetization.

Fourth, the soft magnetic layer on the pill should have a high value of magnetic permeability in order to provide an efficient magnetic flux closure path for the magnetic field created by the hard magnetic layer. This field will be strongly drawn to the pill magnetic layer, thus completing the magnetic circuit and resulting in a sizeable bonding force. Fifth, the soft layer should have low coercivity so it is easily magnetized by the host substrate hard magnetic layer. Sixth, the soft layer should have low remanence to minimize the force between pills that could potentially cause the pills to stick together magnetically. These criteria are shown in Table 2.1.

Property	Hard Magnetic Film	Soft Magnetic Film
$\mathbf{H_c}$	high, > M_r(soft film)	low, < M_r(hard film)
$\mathbf{M_r}$	high, > H_c(soft film)	low, < H_c(hard film)
μ	low	high

Table 2.1 Rough magnetic criteria for MASA functionality.

2.3.2 Magnetic Force Expression

The hard magnetic layer magnetization pattern shown in Figure 2-7 is periodically varying and can be approximated by a sinusoid, $M_y = M_r \cos kx$. With, H = 0, the flux density, B is due entirely to this sinusoidal magnetization. As one moves away from the material, the flux density decays exponentially. Thus,

$$\vec{B} = \mu_O(\vec{H} + \vec{M}) = \mu_O \vec{M} \approx \mu_O[\vec{M_r} \cos kx]e^{-ky}. \qquad (2.2)$$

When the pill with a soft magnetic material approaches the host substrate with its hard magnetic layer having the domain pattern shown in Figure 2-7, the pill is drawn to the target substrate since the soft magnetic film provides an efficient magnetic flux closure path. Ultimately, the force bonding the device pill and target substrate will be so strong that the device will be fully retained at the substrate [13].

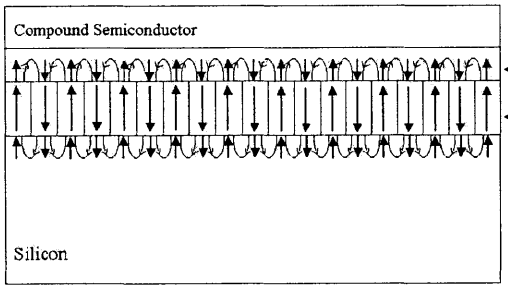

Figure 2-8: Schematic showing the heterostructure pill retained by the target wafer.

By analyzing Maxwell's equations and considering the boundary conditions at the medium interfaces, this pattern has been shown to produce a magnetic force density given by

$$\frac{F}{A} \approx \frac{B_R^2}{\mu_O \pi^2}(1 - e^{-2\pi t_1/L})^2 e^{-4\pi t_2/L} \frac{\sinh(\frac{2\pi t_3}{L})}{\sinh[\frac{2\pi t_3}{L} + \ln\frac{(\mu + \mu_O)}{(\mu - \mu_O)}]} \text{ [13]} \qquad (2.3)$$

where the variables, t_1, t_2, t_3, and L are defined in Figure 2-9.

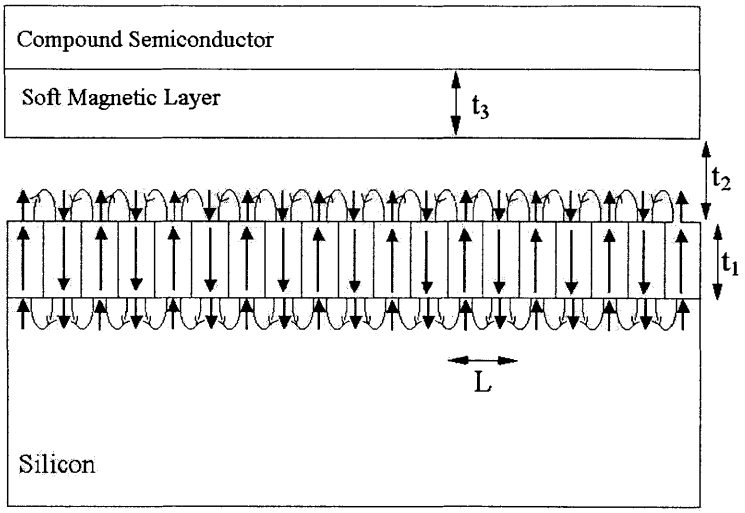

Figure 2-9: Schematic showing the heterostructure pill approaching the target substrate.

Looking at this expression, one can note the similarities with the magnetic material requirements described in Section 2.3.1 by considering the force expression in terms of four multiplying factors. The first factor of the magnetic force density expression, $\frac{B_R^2}{\mu_O \pi^2}$, shows a quadratic dependence on the remanent flux density, B_r. Thus, the hard magnetic film should have as large a remanence as possible. The second component of the force density, $(1-e^{-2\pi t_1/L})^2$, reiterates the importance of the criterion that the hard magnetic film have significant thickness so that the force on the pill due to the top surface will greatly exceed the force due to the bottom surface. The third component, $e^{-4\pi t_2/L}$, relates the exponential decay of the flux density outside of the magnetic film and the fact that this force is significant only for small separations. Finally, the fourth component,

$$\frac{\sinh(\frac{2\pi\ t_3}{L})}{\sinh[\frac{2\pi\ t_3}{L} + \ln\frac{(\mu\ +\mu_O)}{(\mu\ -\mu_O)}]}$$, shows the dependence on the soft magnetic film thickness and typically has a value near unity.

2.4 The Benefits of the MASA Technique

As was discussed in Chapter 1, the three main research efforts in optoelectronic integration are direct epitaxy, wafer bonding, and fluidic assembly. MASA can be considered a fluidic assembly technique. For MASA to be a viable option, it must have significant advantages over the other competitive research approaches.

2.4.1 MASA Advantages over Direct Epitaxy

Since devices are grown on a single substrate, direct epitaxy requires compatible process variables such as etch chemistries and temperatures. Due to the differences in materials utilized, this often results in a compromised process. In comparison, MASA offers higher device quality by enabling the optimum processing of each device being integrated. Moreover, this correlates into greater flexibility concerning which devices are integrated.

MASA also allows for functionality testing of devices prior to integration; whereas direct epitaxy does not. MASA should therefore provide higher overall yield. MASA should allow for a more planar topography than direct epitaxy and thus should prove to be a more high volume manufacturable technology.

2.4.2 MASA Advantages over Wafer Bonding

In comparison to full wafer bonding, MASA offers other advantages. In wafer bonding, all of the devices on a wafer being integrated are coupled together through their substrate. Thus, the stress on one device will be coupled to the other devices. In MASA, the devices being integrated are uncoupled from one another and should not undergo such stresses.

Second, MASA enables the efficient use of semiconductor material. For wafer bonding to be most efficient, the wafers being integrated should have the same diameter. Unfortunately, the industry standard wafer sizes for the different semiconductor materials such as Si, GaAs, and InP differ significantly. For instance, the industry standard Si wafer is typically 8" or 12" in diameter; whereas, GaAs and InP wafers are usually 4" or 6" in diameter. Full wafer bonding would result in a significant waste of semiconductor material. In MASA, since devices are etched free from the substrate and integrated individually, the requirement that device wafer sizes be comparable no longer applies and more efficient use of the semiconductor material occurs [13].

Third, wafer bonding requires some sort of redundancy to provide for the likely scenario that some devices will be non-functional. Since MASA involves integration of individual devices or small array of devices, non-functional devices or device arrays could be screened out prior to integration. Therefore, MASA likely will result in a higher overall yield.

2.4.3 MASA Advantages over other Fluidic Assembly Techniques

In comparison to Fluidic Self Assembly, MASA should provide a much stronger retention force and thus should be better suited to transport through the fab. Moreover, MASA avoids the requirement of patterning the devices in trapezoidal shapes and thus

avoids the process variation that accompanies this patterning. In relation to Electric Field Directed Assembly, MASA removes the need for depositing complex electrode patterns on the target substrate that are only used for integration.

Chapter 3

Magnetics Theory and Characterization Discussion

All materials exhibit some form of magnetism. Depending on their magnetic properties, materials are given such labels as diamagnetic, paramagnetic, or ferromagnetic. When a strong magnetic field is applied to a diamagnetic material, such as gold, the material is magnetized in the direction opposite to the applied field. Paramagnetic materials, such as titanium and chromium, when placed in a strong field can be magnetized in the same direction as the applied field. However, for both diamagnetic and paramagnetic materials, the induced field is weak and disappears when the external field is removed.

The materials utilized for their magnetic properties in MASA are ferromagnetic materials. When placed in a magnetic field, ferromagnetic materials can be magnetized strongly in a direction parallel to the applied magnetic field. In addition, unlike diamagnetic and paramagnetic materials, when the external field is removed, ferromagnetic materials maintain a nonzero magnetization. For magnetic materials, $\vec{B} = \mu_O(\vec{H} + \vec{M})$. For ferromagnetic materials, $\vec{B} \approx \mu_O \vec{M}$.

The only elemental room temperature ferromagnetic materials are Ni, Co, and Fe. A single atom of Ni, Co, or Fe is paramagnetic. However, when many atoms are brought together, a spontaneous nonzero magnetization results from a phenomenon referred to as exchange coupling where electron spins in the partially filled 3d inner sub-shells of

neighboring atoms align. When many atoms are brought together, the partial band of one spin will be lowered in energy by this exchange interaction and the partial band of the opposite spin will be raised in energy by the interaction. Energetically speaking, all of the 3d electrons would like to go to the partial band having the lowest energy. However, due to the Pauli Exclusion principle, some electrons must move to the higher energy opposite spin states. If the energy reduction due to the exchange interaction is larger than the energy increase caused by the Pauli Exclusion principle, then the parallel arrangement of the 3d electron spins is favorable and the material is ferromagnetic.
Above a temperature referred to as the Curie temperature, the electrons gain enough thermal energy to realign their spins and the material loses its ferromagnetic character.

Contained in the following sections is a discussion on the different anisotropies influencing the magnetic properties of magnetic materials. In addition, the magnetic materials used in this initial MASA research and their measured properties are discussed along with the techniques used to extract these characteristics.

3.1 Magnetic Anisotropy

Magnetic anisotropy describes the phenomena where magnetic properties depend on direction in the material. Magnetic anisotropy can result from material crystalline structure (magnetocrystalline anisotropy), shape (shape anisotropy), strain (magnetoelastic anisotropy), or interface effects (surface anisotropy). The relative strength of these anisotropies is understood by performing a comparison of the magnetic energy densities related to these anisotropies. If a certain magnetic anisotropy energy density is significantly larger than the other magnetic anisotropy energy densities, then this anisotropy will dominate and the magnetization direction in the magnetic material will be determined by this anisotropy.

3.1.1 Magnetocrystalline Anisotropy

The magnetic properties of materials are often favored along certain crystal directions. This phenomenon is referred to as magnetocrystalline anisotropy. As an example, magnetization in nickel, is favored along the [111] direction, which is referred to as the easy direction; whereas, the [100] direction is less favored and is referred to as a hard direction. An idea of the size of the magnetocrystalline anisotropy energy density can be gained from the magnitude of the first and second-order magnetocrystalline anisotropy constants, K_1 and K_2 [14].

3.1.2 Shape Anisotropy

Shape anisotropy describes the phenomenon where it is energetically favorable for the magnetization in a magnetic material to occur along long dimension directions as opposed to short dimension directions (Figure 3-1). If the magnetization aligns along the long dimension direction, the number of surface magnetic poles and thus the magnetic flux leaving the magnetic material will be minimized. Magnetic flux lines penetrating the magnetic material surface result in significant energy costs and are thus not favored.

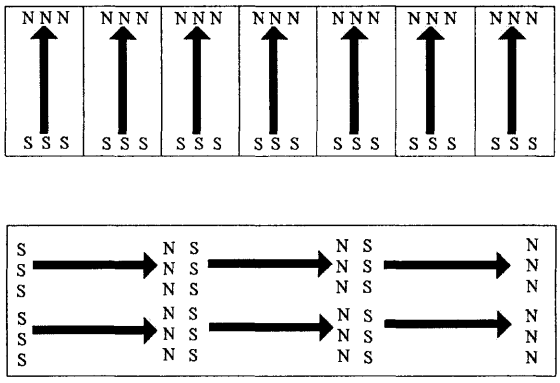

Figure 3-1: Sample magnetized (a) out-of-plane, (b) in-plane.

Shape anisotropy is further explained by considering the concept of a demagnetizing field. The demagnetization field is approximated by the expression $H_d = -N\vec{M}$, where N is the demagnetization factor dependent on the sample dimensions, and $\vec{M}$ is the material magnetization. The orthogonal demagnetization factors in a sample must add up to unity, $N_x + N_y + N_z = 1$. In whatever direction a field is applied, a demagnetizing field is present within the sample that acts in a direction opposite to the applied field. Demagnetizing factors along short dimensions in a material are larger than the corresponding factors along long sample dimensions. This quantifies the difficulty in magnetizing a sample along a short direction. The magnetostatic, or shape anisotropy energy density can be approximated by

$$E_{shape} = -\mu_O \vec{M} \cdot \vec{H_d} = \frac{\Delta N}{2} \mu_O M_S^2 \cos^2 \theta , \qquad (3.1)$$

where θ is the angle between the magnetization $\vec{M}$ and the applied field, $\vec{H}$, and ΔN is the difference in demagnetizing factors in the two orthogonal directions [15].

3.1.3 Magnetoelastic Anisotropy

Magnetoelastic anisotropy describes the effect where the stress that a magnetic material undergoes can affect the direction in which the magnetization easily aligns. This is especially important if a thin crystalline ferromagnetic material is grown on a lattice mismatched substrate. The approximate size of the magnetoelastic energy density can be estimated by knowing the size of the product of the strain in any of the three orthogonal directions, e_{xx}, e_{yy}, and e_{zz} and the first order magnetoelastic anisotropy constant, B_1, or the product of any of the shear strains, e_{xy}, e_{yz}, or e_{zx} and the second order magnetoelastic anisotropy constant, B_2 [15].

3.1.4 Surface Anisotropy

When very thin layers of magnetic materials are involved, a fourth type of anisotropy referred to as surface anisotropy could dominate. At materials' surfaces, there is a reduced symmetry in terms of electronic structure. In other words, there is a low probability for electrons at the surface to move in a direction perpendicular to the surface since it is unlikely for electrons to escape the material. In the bulk, the electrons can move in any direction because of the symmetry involved.

Therefore, at the surface, it is probable that the electrons will move in the plane of the surface. Electrons moving in directions that are in the plane of the surface have orbital angular momentum components that are directed out of the plane of the surface. This is believed to cause the magnetization to preferentially align perpendicular to the plane of the film and is referred to as surface or interface anisotropy. The surface anisotropy energy density is inversely proportional to the thickness of the magnetic film and directly proportional to the surface anisotropy constant, K^S, which is a constant of the material being investigated [15,16].

3.2 Thin Film Ferromagnetism

Given a sample's composition and dimensions, it is possible to qualitatively estimate what anisotropies will be most influential and in which directions the magnetizations will align easily. To do this analysis, the magnetic energies related to these anisotropies are considered.

Based on energy considerations, for thin films, shape anisotropy is a very significant component of magnetic energy. The demagnetization factors for a thin film sample (Figure 3-2), are approximately $N_z \approx 1$, $N_x \approx 0$, and $N_y \approx 0$. Thus, due to shape anisotropy, the film is most easily magnetized in the plane of the film. Magnetizing with a magnetic field perpendicular to the plane results in a demagnetizing field having the

value $H_d = -NM_s\cos\theta = -M_s\cos\theta$, where θ is the angle between the direction of the magnetization, $\vec{M}$, and the applied field, $\vec{H}$. The shape anisotropy energy density for magnetizing the thin film out-of-plane is estimated to be

$$E_{shape} = -\mu_O \vec{M} \cdot \vec{H}_d = \frac{\Delta N}{2} \mu_O M_S^2 \cos^2\theta = \frac{1}{2} \mu_O M_S^2 \cos^2\theta \qquad (3.2)$$

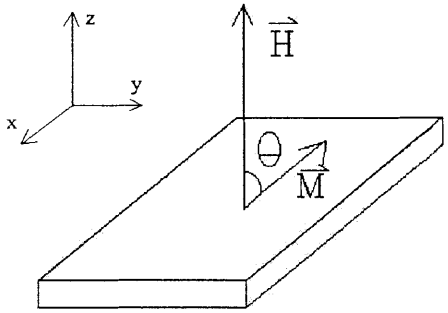

Figure 3-2: Thin film sample with dimensions $d_x \approx d_y >> d_z$.

The magnetization, $\vec{M}$, can be rotated from a direction in-plane to a direction out-of plane by applying a strong enough magnetic field in a direction perpendicular to the plane of the film. However, when that magnetic field is removed, the magnetization vector will rotate back to its energetically favorable orientation in the plane of the film due to the shape anisotropy.

Therefore, if an out of plane magnetization is desired in a thin film, the sample must have significant out-of-plane magnetocrystalline, magnetoelastic, or surface anisotropy to combat the in-plane preferred shape anisotropy. If non-epitaxial films are used, as in the case of sputtered films, the sample must have significant out-of-plane magnetoelastic or surface anisotropy. For these anisotropies to be significant enough, the sample should be significantly thin (i.e., only a few atomic layers).

In order to use shape anisotropy to generate films with a preferential out-of-plane magnetization, the sample should be patterned so that the in-plane dimensions are on the order of or smaller than the vertical dimension.

3.3 MASA Magnetic Layer Characteristics

3.3.1 Magnetic Material Characterization Methods

As was described in Chapter 2, the essential properties of magnetic materials, such as remanent magnetization, coercivity, and saturation magnetization, can be extrapolated from a hysteresis loop. Vibrating sample magnetometry (VSM) is the technique widely used to generate a sample's hysteresis loop and thus ascertain the sample's associated quantitative magnetic properties. Torque magnetometry can be used to deduce a sample's magnetic anisotropy. In addition, a visual profile of the magnetic fields near the surface of sample can be gained from magnetic force microscopy (MFM). In the characterization carried out thus far of the magnetic materials used in MASA, VSM and MFM have been the main techniques used while torque magnetometry has been used to a lesser extent.

3.3.1.1 Vibrating Sample Magnetometry (VSM)

A Digital Measurement Systems vibrating sample magnetometer (VSM) has been used to measure the hysteresis loops of the magnetic materials used in this MASA research effort. As is shown in Figure 3-3, a VSM consists of a large electromagnet that is used to apply a DC magnetic field to a sample that is vibrated in the gap in between the electromagnet. By placing a magnetic material in a magnetic field, an additional magnetic flux due to the sample's magnetization is generated. Operating on the principle of Faraday's law, the sample is vibrated to make this magnetic induction time variant so that sensing coils can be used to detect this varying magnetic induction and generate a

voltage in response. With the magnetic induction, B, measured, and the applied field H known, the magnetization M is determined by the VSM software where $\vec{B} = \mu_O(\vec{H} + \vec{M})$

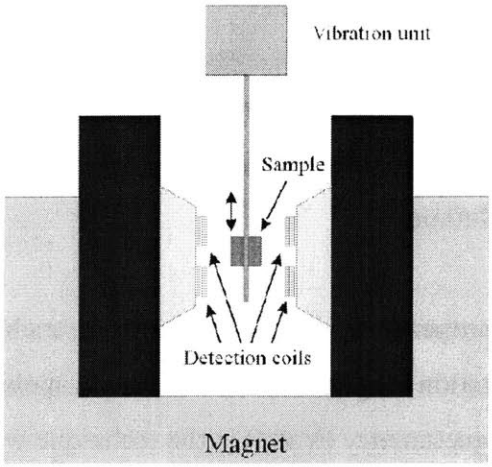

Figure 3-3: Vibrating Sample Magnetometer (VSM) operation schematic [17].

Operating on the principle described above, typical operation of the VSM would involve the sweeping of the applied magnetic field over a user-defined range from –10 kOe to 10 kOe in increments of 200 Oe. The applied magnetic field would then be re-swept over a range of 10 kOe to –10 kOe in steps of –200 Oe. At each applied magnetic field value, the magnetization is determined using the technique described above. From this matrix of data, the magnetization as a function of applied magnetic field, otherwise known as the hysteresis loop is plotted.

3.3.1.2 Magnetic Force Microscopy (MFM)

Magnetic Force Microscopy (MFM) has been used to image the magnetic fields associated with thin film samples. In MFM, a thin cantilever coated with a magnetic film such as cobalt is scanned approximately 100 nm above a sample. During scanning, the tip is vibrated at its resonance frequency. If the magnetic field emanating from the sample is strong enough, the magnetic probe tip is deflected. This deflection corresponds

to a shift in the resonance frequency of the cantilever that is measured by laser detection [18]. A schematic of the MFM setup is shown in Figure 3-4.

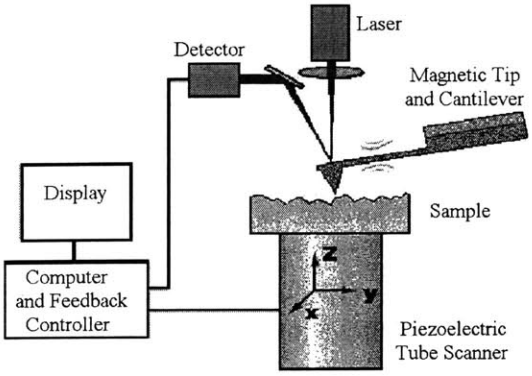

Figure 3-4: Magnetic Force Microscope (MFM) operation schematic [18].

3.3.1.2.1 Magnetic Domain Imaging

A ferromagnetic material is comprised of many microscopic regions called domains. Within a domain all magnetic moments are aligned and thus a net magnetization is associated with it. Domains form in order to minimize the energy that occurs when magnetic flux components perpendicular to the surface of the magnetic layer exist. Magnetic force microscopy is the preferred technique for imaging domains since magnetic force microscopy images the magnetic field emanating from the sample. Figure 3-5 shows the case of a 180° domain wall where two oppositely oriented domains are situated side by side. The magnetization vector cannot switch abruptly to anti-parallel orientations between the two domains, but instead there is an exchange length over which the magnetization vector transitions. To accommodate this domain orientation, there will be some fringe field that must occur over some exchange length. MFM can detect this fringe field and can thus image the domain pattern.

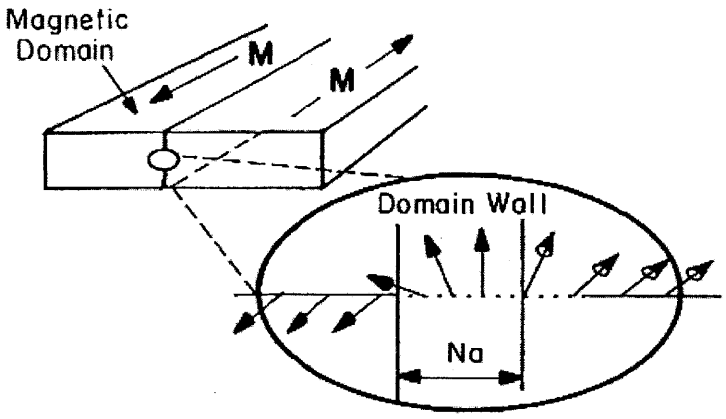

Figure 3-5: Schematic showing a 180° domain wall and the length over which the magnetization vector rotates potentially causing some fringe field detectable by an MFM [15].

Figure 3-15 shows an MFM image of a nickel film on a GaAs substrate. The light and dark images correspond to domains. These domains can be imaged by the deflection of the MFM cantilever due to the fringe magnetic field existing above the film. This fringe field is necessary due to the fact that adjacent domains have different magnetization orientations and to accommodate this the magnetization must transition over a small exchange length. This concept is theorized in Figure 3-5.

3.3.1.3 Torque Magnetometry

The experimental setup in torque magnetometry involves the suspension of the sample under test in the gap between an electromagnet. A DC magnetic field is applied as the sample is rotated. The torque density can be expressed as the first derivative of the magnetic energy density, described earlier in this chapter, with respect to the angular rotation, θ.

$$T = -\frac{\partial E}{\partial \theta} \quad [19]. \tag{3.3}$$

3.3.2 Magnetic Properties of the Hard Magnetic Layer

As was discussed in Chapter 2, the hard magnetic material on the target wafer should have certain characteristics for the MASA technique to be viable. Foremost among these is an out-of-plane magnetization with significant remanence. As has been discussed, obtaining thin films with out-of-plane magnetization is challenging due to the dominance of shape anisotropy that favors in-plane magnetization. Thus, a few material systems were investigated in search of a suitable hard magnetic layer that acts as the permanent magnet in the MASA technique. All of the materials investigated are cobalt based due to cobalt's hard magnetic properties and high saturation magnetization. The two structures considered were a sputter deposited cobalt (Co)/palladium (Pd) multi-layer film that was patterned into an array of bars, and an electrodeposited Co film on gold (Au) that was not patterned.

3.3.2.1 Co/Pd System

It was discovered in the late 1980s that by depositing alternating layers of ultra-thin cobalt and palladium that a sample with a preferred direction of magnetization out-of-plane could be realized [20]. Since then, the Co/Pd multi-layer system has been studied extensively for the potential use as high-density perpendicular magnetic storage media [21, 22].

The preferential out-of-plane magnetization has been theorized over the years to be a result of the surface anisotropy that is produced by the ultra-thin layers of Co/Pd [16,23,24]. Typically, the Co/Pd system is modeled in terms of the magnetic energy densities corresponding to magnetocrystalline, magnetoelastic, shape, and surface anisotropy,

$$E_{total} = E_{MC} + E_{Shape} + E_{ME} + E_{sur} \tag{3.4}$$

$$E_{total} = K_u^{mc} \sin^2\theta - \frac{\mu_O M_S^2}{2}(\sin^2\theta - 1) + B_1 e(2\sin^2\theta - 1) + \frac{2K^S}{t_{Co}}\sin^2\theta \quad (3.5)$$

$$E_{total} \approx K_u^{Co}\sin^2\theta, \quad (3.6)$$

where $K_u^{Co} = K_u^{mc} + 2B_1 e - \frac{\mu_O M_S^2}{2} + \frac{2K^S}{t_{Co}}$.

In order for perpendicular magnetization to be favored, K_u^{Co} must be a positive number. Engel et al. measured the anisotropy constant K_u^{Co} as a function of cobalt film thickness and plotted (K_u^{Co} t_{Co}) as a function of t_{Co} as is shown in Figure 3-6.

$$K_u^{Co} t_{Co} = (K_u^{mc} - \frac{\mu_O M_S^2}{2} + 2B_1 e)t_{Co} + 2K^S \quad (3.7)$$

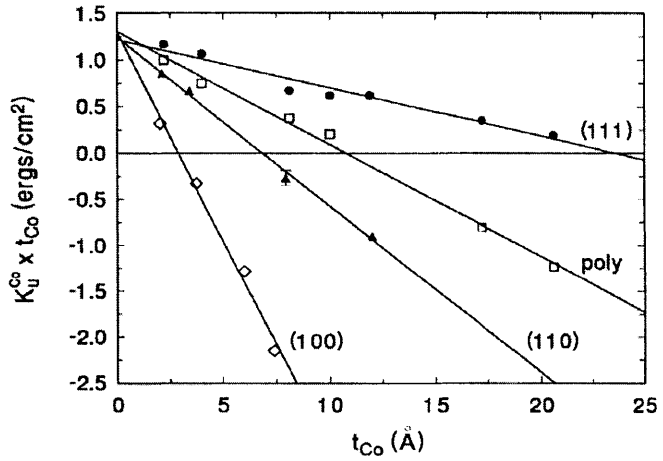

Figure 3-6: Out-of-plane anisotropy constant and cobalt layer thickness product as a function of cobalt layer thickness for both single crystal and polycrystalline Co/Pd multi-layers [23].

Figure 3-6 shows that surface anisotropy is independent of crystal structure and the anisotropy constant has an approximate value of $K^s \approx 0.65$ mJ/m^2 for the Co/Pd interface.

Moreover, for all Co/Pd multi-layer films it is possible to obtain films with preferred out-of-plane magnetization as long as the film is sufficiently thin.

In this initial MASA research effort, a 250 period thick Co/Pd multi-layer film was sputter deposited and patterned into a pattern of bars and spaces having a period of approximately 2 um by Prof. T.C. Chong's group at the Data Storage Institute on the campus of the National University of Singapore. Atomic force microscope images of these bars are shown in Figure 3-7 and Figure 3-8. Each cobalt layer in the film has a thickness of approximately 0.28 nm, whereas each palladium layer has a thickness of about 0.6 nm. The overall thickness of the Co/Pd film is thus 220 nm.

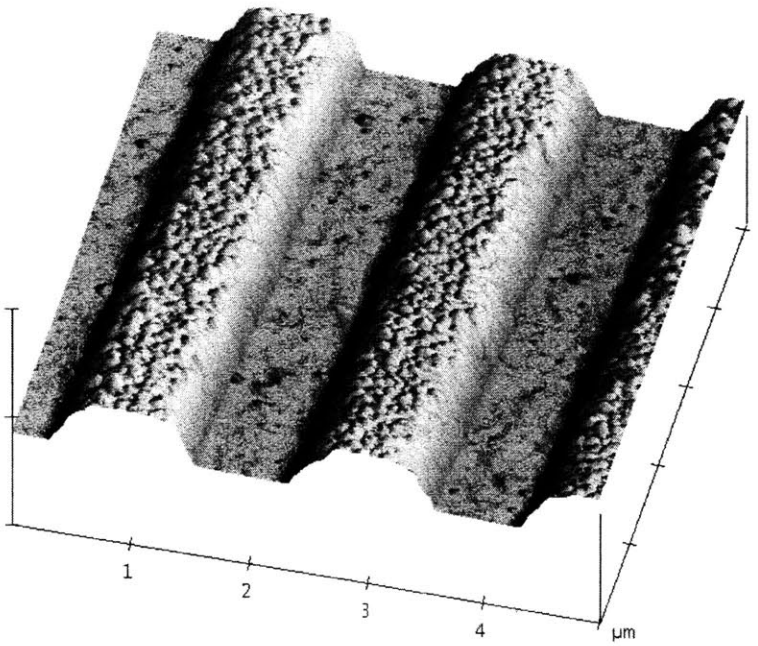

Figure 3-7: Atomic Force Microscope image showing bar dimensions of a Co/Pd sample sputter deposited and patterned by Prof. T.C. Chong's group at the Data Storage Institute on the campus of the National University of Singapore.

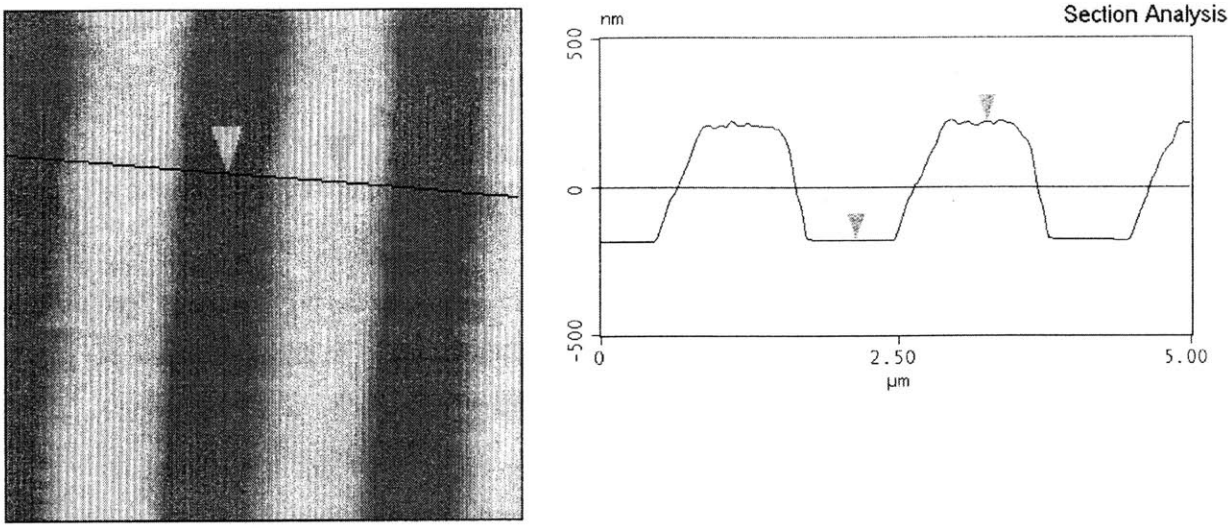

Figure 3-8: Atomic Force Microscope image showing the thickness characteristics of a Co/Pd sample sputter deposited and patterned by Prof. T.C. Chong's group at the Data Storage Institute on the campus of the National University of Singapore.

Magnetic hysteresis loop measurements have been performed on these samples. Figure 3-9 confirms that the out-of-plane direction is the preferred easy magnetization direction with significantly higher remanence than the in-plane direction.

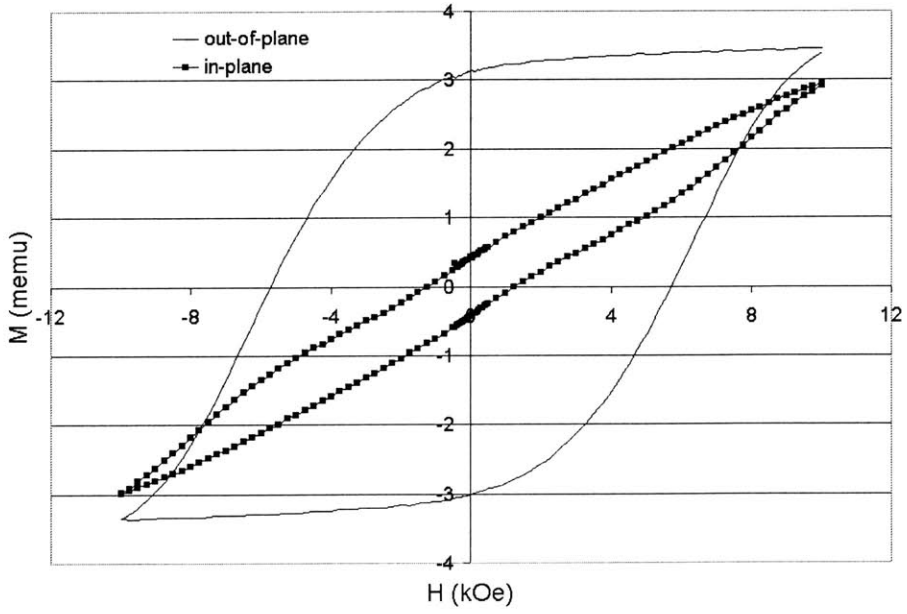

Figure 3-9: Sputter deposited and patterned 250 period thick Co(0.28 nm)/Pd(0.6 nm) multi-layer film magnetic hysteresis loop.

The magnetic field above the sample was imaged with a force microscope by scanning at a height of 100 nm over the Co/Pd sample with both a magnetic and non-magnetic probe with the results shown in Figure 3-10. The increased contrast observed with the magnetic probe shows the contribution of the magnetic force.

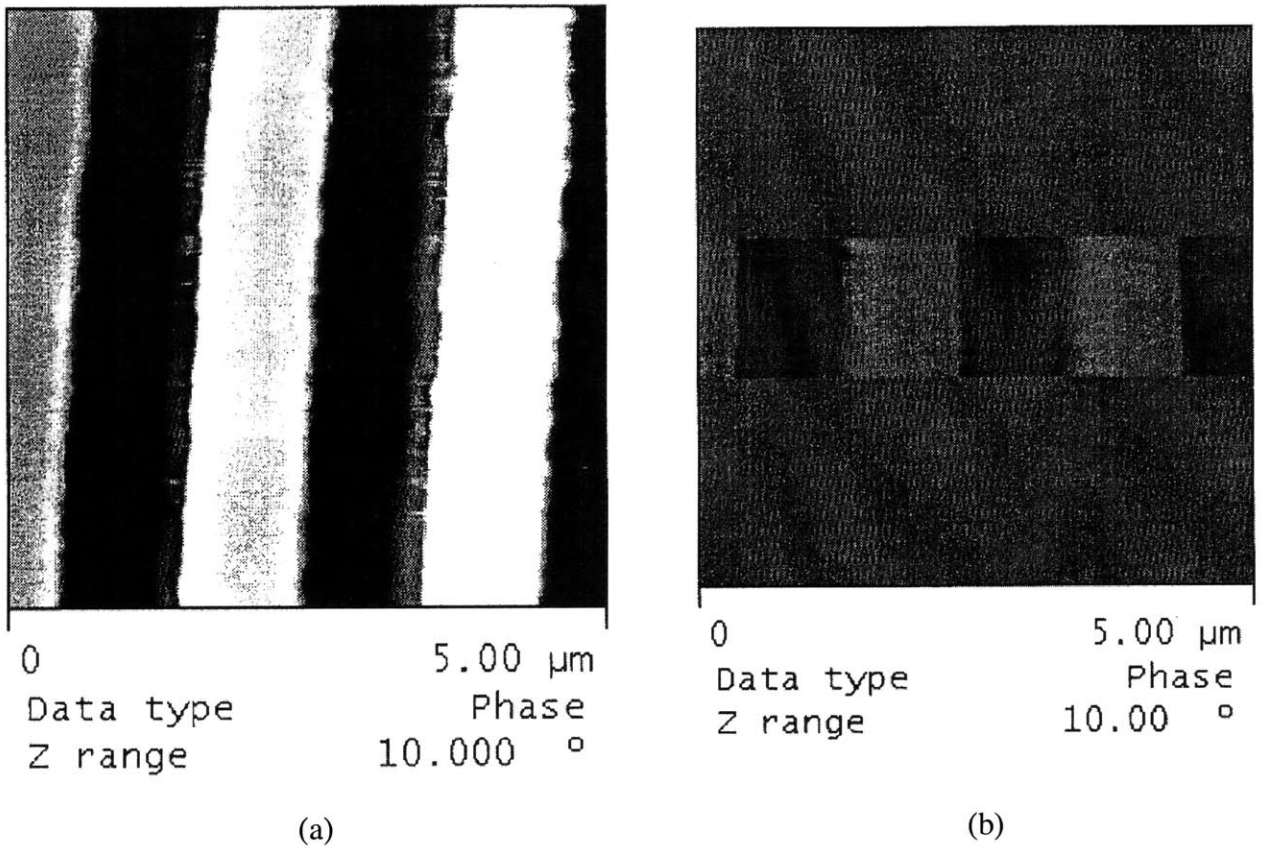

(a) (b)

Figure 3-10: Force microscope phase measurement demonstrating the magnetic force due to the Co/Pd patterned multi-layer film: (a) Phase image obtained using magnetic tip, (b) Phase image obtained using standard non-magnetic tip.

3.3.2.2 Co/Au System

As the Co/Pd multi-layer structure is an extremely complicated structure to fabricate, the magnetic properties associated with single film layers were investigated. Specifically,

cobalt was electrodeposited onto a gold seed layer. The magnetic hysteresis loop measured for this structure is shown in Figure 3-11. As expected, this shows a definite preference for in-plane magnetization. Moreover, the in-plane and out-of-plane coercivities of around 150 Oe are quite low.

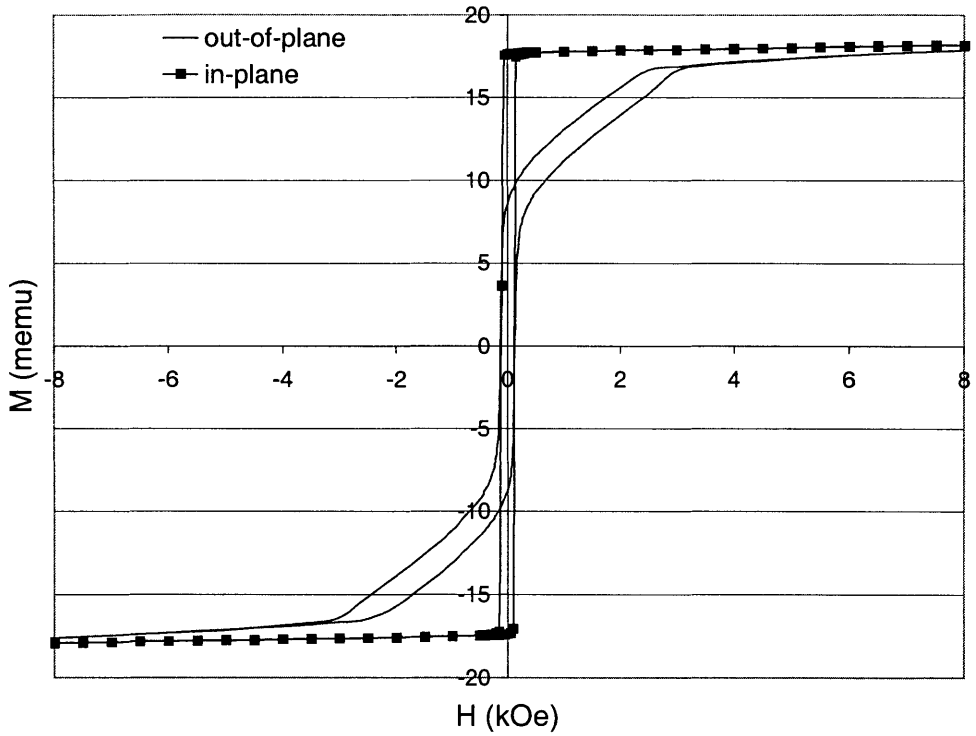

Figure 3-11: Magnetic hysteresis loop of an electrodeposited cobalt thin film on a gold substrate.

It may be possible to use electrodeposited cobalt as the hard magnetic layer if cobalt can be electrodeposited with thickness greater than the in-plane dimensions to take advantage of shape anisotropy and result in an out-of-plane preferred magnetization. Unfortunately, an unpatterned cobalt thin film will not suffice.

3.3.3 Magnetic Properties of the Soft Magnetic Layer – Ni/GaAs structure

3.3.3.1 Sputter Deposited Nickel on GaAs

Nickel was chosen as the soft magnetic film for the initial demonstration of the MASA technique. The normalized in-plane and out-of-plane magnetic characteristics of a sputtered nickel on GaAs sample are shown in Figure 3-12. Looking at the bulk properties of nickel shown in Table 3.1, one sees that the shape anisotropy has a magnitude that is two orders of magnitude larger than the magnetocrystalline anisotropy. Furthermore, since the nickel is sputter deposited, a polycrystalline nickel film results. This further weakens the magnetocrystalline anisotropy.

$u_o(M_s)^2/2$	**Shape anisotropy constant**	$+1.4 \times 10^5$ J/m^3
K_1	**1st order crystal anisotropy constant**	-4.5×10^3 J/m^3
K_2	**2nd order crystal anisotropy constant**	$+2.3 \times 10^3$ J/m^3
B_1	**1st order magnetoelastic anisotropy constant**	$+6.2 \times 10^6$ N/m^2
B_2	**2nd order magnetoelastic anisotropy constant**	$+4.3 \times 10^6$ N/m^2

Table 3.1: Bulk nickel magnetic constants [15].

Due to this large shape anisotropy, the easy direction for magnetization is in-plane. However, some out-of-plane magnetization is favored as the out-of plane hysteresis loop has a non-zero remanence.

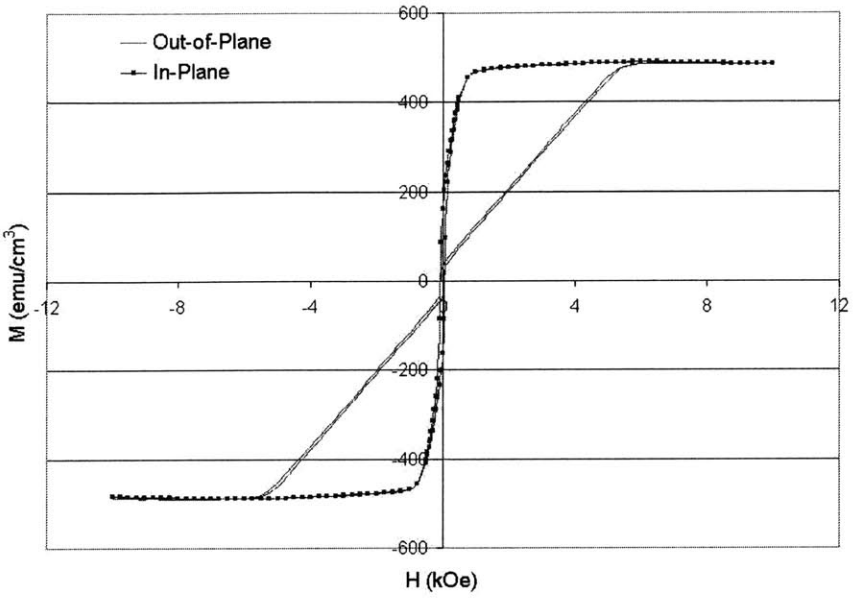

Figure 3-12: Magnetic hysteresis loop of a 0.38 um sputter deposited nickel film on a GaAs substrate.

The out-of-plane remanent magnetization for a sputter deposited 0.38 um nickel film on GaAs substrate was measured to be approximately 33 emu/cm^3 and is shown in Figure 3-13.

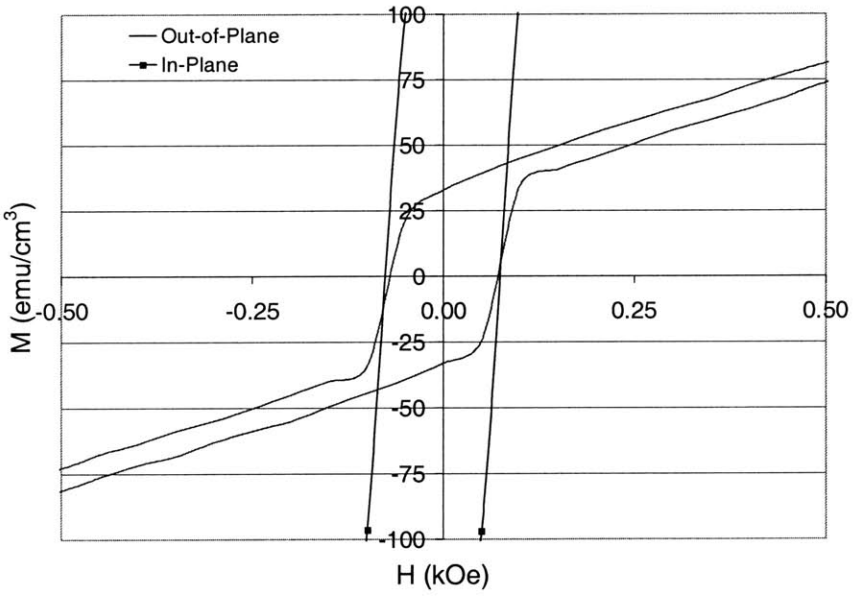

Figure 3-13: Close-up of the magnetic hysteresis loop of a sputter deposited 0.38 um nickel film on a GaAs substrate.

A VSM measurement was performed on a 0.28 um sputter deposited nickel film on GaAs substrate sample yielding similar hysteresis loop results. The preference for in-plane magnetization was confirmed by torque magnetometry measurements performed on the 0.28 um Ni/GaAs sample as is shown in Figure 3-14. The magnetic easy and hard axes correspond to the locations where the torque becomes zero with a negative and positive slope respectively. Thus, the hard axis is very near 90° showing that the hard axis is close to if not exactly in-plane.

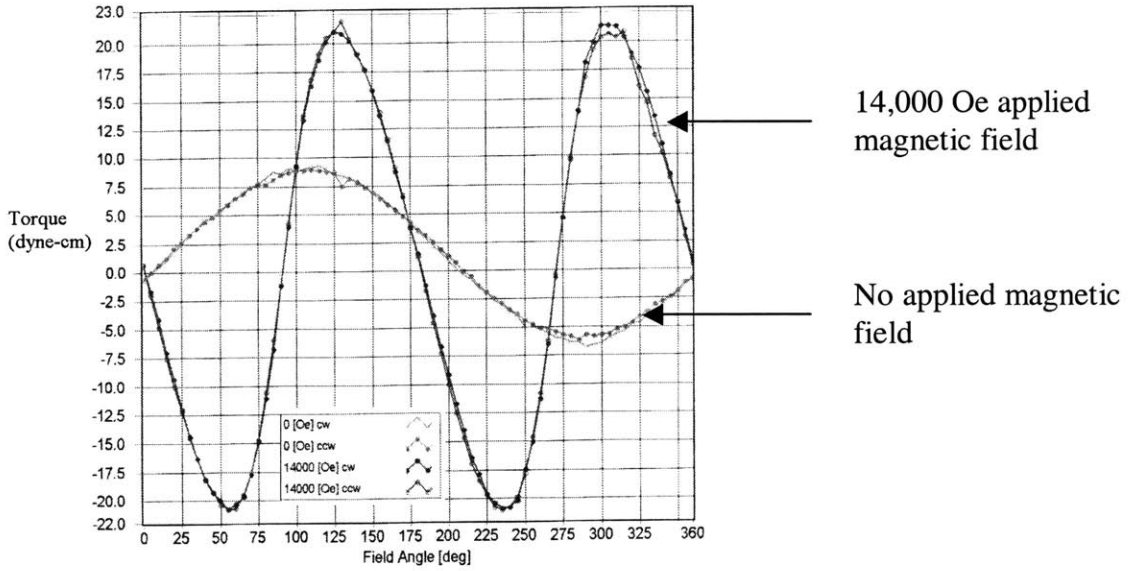

Figure 3-14: Torque magnetometry plot of a sputter deposited Ni (0.28 um)/GaAs sample showing slight out-of-plane remanent magnetization.

A slight portion of the magnetization remaining in the out-of-plane direction can be understood by considering the previously discussed magnetic anisotropies. Since the nickel film thickness is appreciably smaller than the length and width of the sample (width, length > 1000 x thickness), the shape anisotropy should be significant. Therefore, another anisotropy must be significantly large to offset this shape anisotropy that favors in-plane magnetization. Since the nickel film was sputtered, the sample is polycrystalline and thus the magnetocrystalline anisotropy should be weak. Since, the nickel thickness is not ultra-thin, the surface anisotropy should be negligible. That leaves magnetoelastic anisotropy as the probable cause with the stress resulting from the cooling

down of the samples following sputter deposition. This temperature gradient likely causes significant stress due to the thermal expansion coefficient mismatch of materials. More work needs to be done to conclusively prove that this is the cause of the nonzero out-of-plane remanence, but at present this is the hypothesis.

The results obtained with VSM showing a small remanence in the out-of-plane were verified by performing magnetic force microscope imaging (MFM) on the sample. The results, shown in Figure 3-15, reveal a periodic ripple domain pattern.

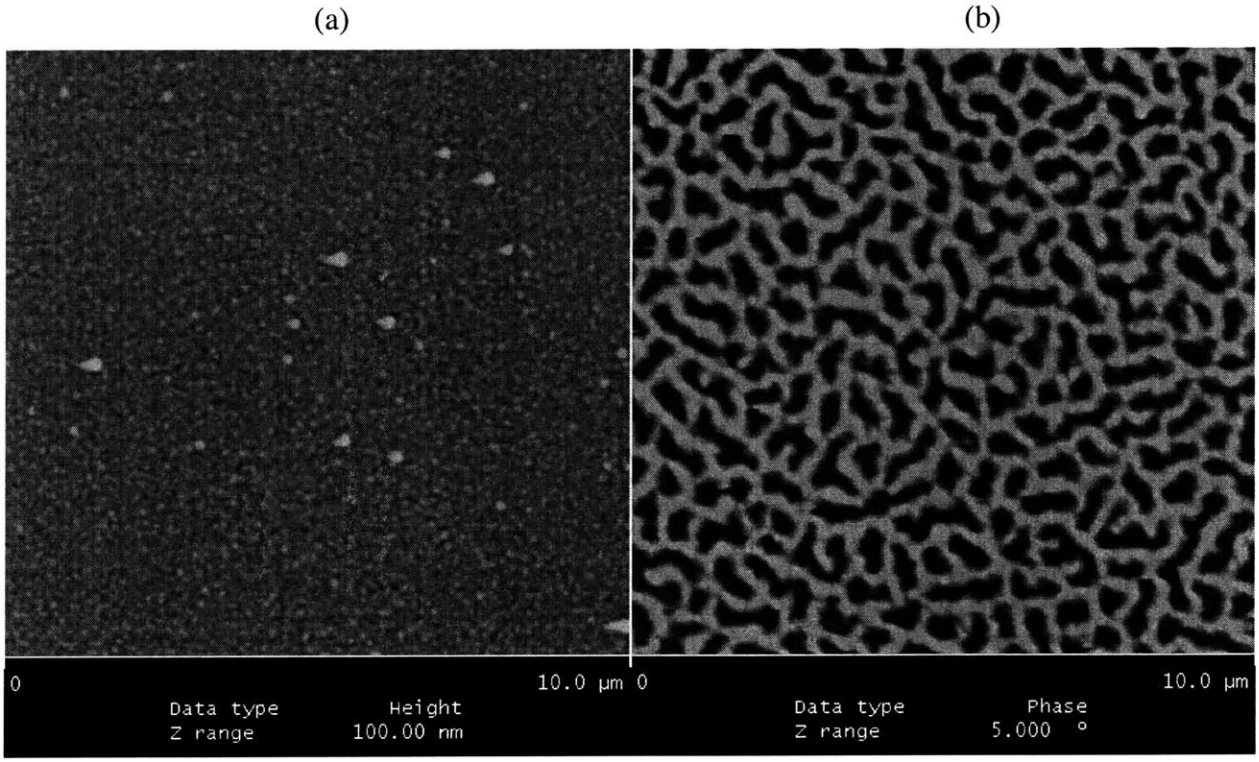

Figure 3-15: Magnetic Force Microscope image of a sputter deposited Ni (0.38 um)/GaAs sample revealing the magnetic domain structure: (a) Height image showing very minor topography on the sample, (b) Phase image showing a ripple magnetic domain pattern.

3.3.3.2 Electrodeposited Nickel on GaAs

Results similar to the sputter deposited nickel samples on GaAs were realized in the analysis of an electrodeposited nickel on an n^+ doped GaAs substrate. The in-plane and

out-of-plane characteristics are shown in Figure 3-16. As with the sputter deposited sample, the most interesting detail is the nonzero remanence seen in the out-of-plane characteristic.

Since both methods of deposition, sputter deposition and electrodeposition, provide very similar magnetic characteristics, these techniques should from a magnetics standpoint be able to be used interchangeably in the MASA execution. The Co/Pd hard magnetic layer may not be able reach the 5 kOe magnetic field required to saturate the nickel film. However, the magnetization induced in the nickel sample should be close to the saturation value though and it is believed that this will be sufficient.

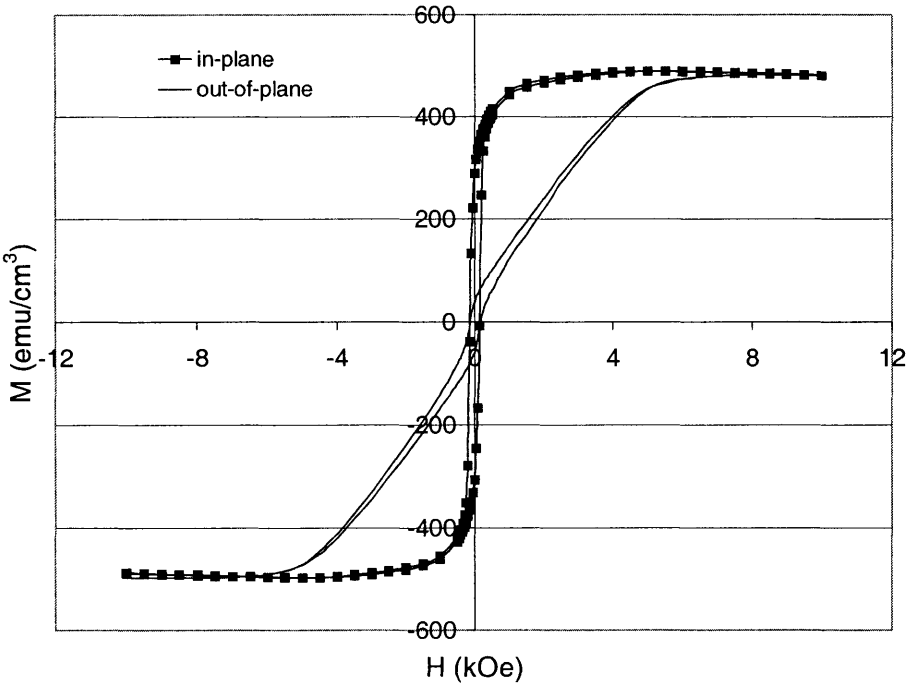

Figure 3-16: Magnetic hysteresis loop of an electrodeposited nickel thin film on an n^+ GaAs substrate.

The out-of-plane remanent magnetization for an electrodeposited nickel film on n^+ GaAs substrate was measured to be approximately 37 emu/cm^3 and is shown in Figure 3-17 which is a close-up image of the hysteresis loop in Figure 3-16.

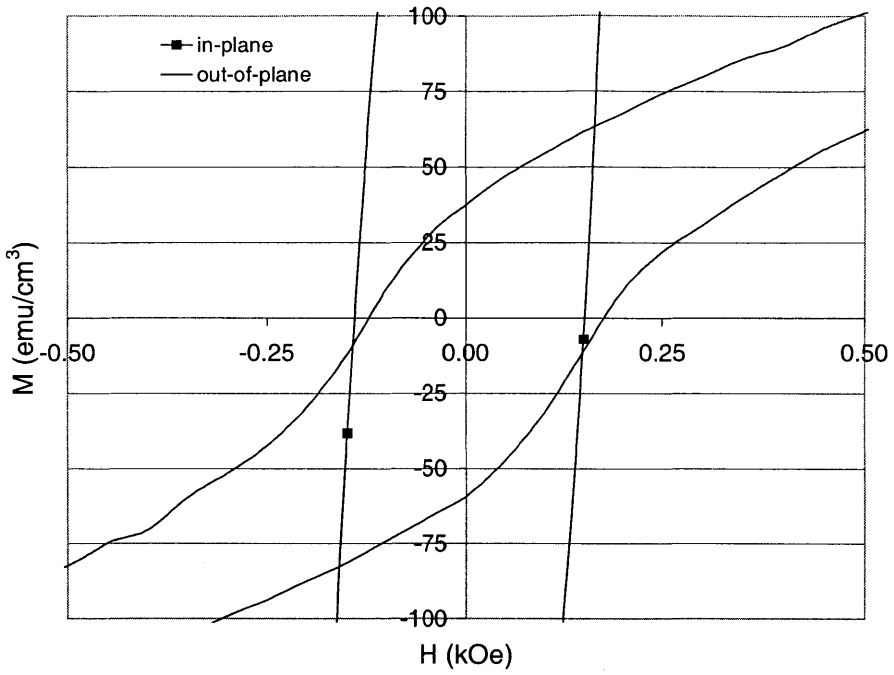

Figure 3-17: Close-up of the magnetic hysteresis loop of an electrodeposited nickel thin film on an n^+ GaAs substrate.

Chapter 4

MASA Process Execution

With the required MASA magnetic criteria established and the magnetic properties of the magnetic films characterized, the process technology for patterning the pills on the heterostructure diode substrate and defining the dielectric recesses on the target substrate had to be developed. Many commercially standardized processing techniques such as reactive ion etching and plasma enhanced chemical vapor deposition were utilized in this development. This chapter summarizes the approaches taken, the difficulties encountered, and the solutions implemented in this process technology development.

4.1 Ferromagnetic Material Patterning Options

To obtain very anisotropic features in modern semiconductor processes, dry etching techniques such as reactive ion etching (RIE) are often used. The RIE process involves the creation of a plasma in a low pressure chamber. An appropriate plasma gas is chosen that reacts chemically with the material to be etched. An applied electric field directs the plasma ions toward the substrate where they physically and chemically etch the material on the wafer. Common materials used in microelectronics, such as SiO_2, Al, Ti, and Si_3N_4, have well-established RIE chemistries.

Unfortunately, dry chemical etching techniques, such as RIE, have not been found to work for ferromagnetic materials. Specifically, for nickel and iron, the most often used RIE gases, chlorine-based and fluorine-based, do not form volatile reaction products at temperatures less than 200 °C and etching success above these temperatures is questionable [25].

Thus, to fabricate patterned magnetic structures for the Magnetically Assisted Statistical Assembly technique, both the additive process of electrodeposition, and a subtractive process consisting of sputter deposition and sputter etching have been attempted. Each method has its own benefits and drawbacks. The electrodeposition technique requires less process steps than the subtractive process. However, the sputter deposited film is typically more uniform than that achieved using electrodeposition. Wet chemical etching has also been attempted for patterning the magnetic films; however, a number of problems including surface wetting issues and a proclivity for lateral etching over vertical etching were seen [26].

4.2 Magnetic Layer Definition – Additive Process

4.2.1 Electrodeposition Background Theory

The main processing technique employed in the additive process is electrodeposition. Electrodeposition is a useful way of selectively depositing materials at fast rates. This technique is widely used in the magnetic recording industry for thin film head fabrication [27] as well as in state of the art microelectronic interconnect processes where very thick metal layers are deposited in high aspect ratio vias [28].

A schematic of the electrodeposition setup is shown in Figure 4-1.

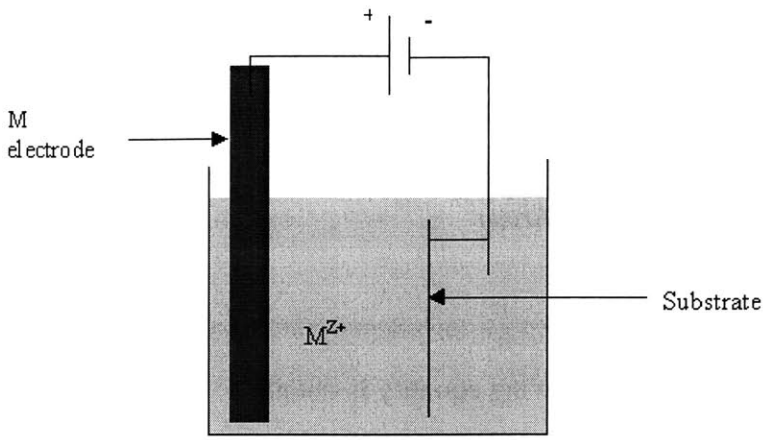

Figure 4-1: Electrochemical cell setup for electrodeposition consisting of a solution containing the salt, M^{Z+}, of the material, M, to be electroplated, a soluble anode made of the material M, a target substrate onto which the plating will occur, and a power supply biasing the cell as shown.

As is shown in Figure 4-1, the electrodeposition process occurs in a bath comprised of a salt, M^{Z+}, of the material, M, to be electroplated. The electrode used is either made of a non-soluble material or a soluble piece of the material to be electroplated. Since the deposition of material from the bath causes depletion of the bath constituents, using a soluble electrode allows the bath constituents to be replenished easily.

The rate at which electrodeposition occurs can be determined from Faraday's law. Faraday's law explains that the size of the electrochemical reaction depends on the charge that passes through the electrochemical cell. Given the reaction $M^{Z+} + Ze^- \rightarrow M$, the electrodeposition of one mole of M, requires Z moles of electrons. Thus, the required charge to complete this reaction is $Q = ZqN_a$, where q is the charge of an electron, and N_a is Avogadro's number. According to Faraday's law there exists a proportionality between the number of moles of product M and Q, the charge passing through the electrochemical cell. The number of moles desired can be converted to a mass as long as the molecular weight of the electrodeposited material is known. Thus,

$$mass_M \ \alpha \ Q(MW_M) \tag{4.1}$$

If the density, ρ_M, and the area to be plated, (Area), are known the following proportionality involving the thickness of the electrodeposit can be derived

$$thickness_M \ \alpha \ \frac{It(MW_M)}{\rho_M (Area)}, \tag{4.2}$$

where I is current and t is time.

Dividing by the charge, Q, the following equality is obtained

$$thickness = (effic.)\frac{(It)(MW_M)}{(Area)(\rho_{Mi})ZqN_a}, \tag{4.3}$$

where effic. is the efficiency factor and accounts for the fact that the process may not be 100% efficient [29].

4.2.2 Target Substrate Hard Magnetic Layer

Cobalt was chosen for its hard magnetic properties and for the ease with which it is electroplated. Cobalt electrodeposition solutions are typically comprised of cobalt (II) sources, such as cobalt chloride, $CoCl_2$, or cobalt sulfate, $CoSO_4$. Boric acid, H_3BO_3 is typically used as a buffer [30].

The plating bath composition and operating parameters used in this thesis work are shown in Table 4.1.

Constituent	**Composition**
$CoCl_2$ $6H_2O$	375 g/l
H_3BO_3	37.5 g/l
temperature	room
pH	3.6
current density	~ 20 mA/cm^2
anode	cobalt

Table 4.1 Cobalt electroplating bath constituents and operating parameters.

The setup of the cobalt electrodeposition process is shown in Figure 4-2 along with the reactions occurring at the cobalt electrode and target substrate as a voltage with specified polarity is applied.

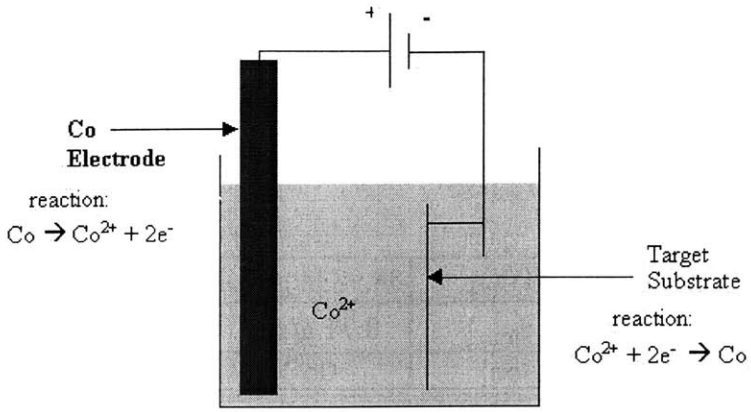

Figure 4-2: Cobalt electrochemical cell denoting the reactions occurring at the anode and the cathode.

When current is passed through the setup, the $CoCl_2$ solution undergoes the ionizing reaction

$$CoCl_2 \rightarrow Co^{2+} + 2Cl^-. \tag{4.4}$$

The positively charged Co^{2+} ions in the solution are electrostatically attracted to the negative voltage anode, whereas the Cl^- ions are attracted to the cathode. At the cobalt electrode, the oxidation reaction

$$Co \rightarrow Co^{2+} + 2e^- \tag{4.5}$$

occurs. These Co^{2+} ions enter the solution and replenish the Co^{2+} ions that are being taken from the solution for plating.

At the target substrate, the reduction reaction

$$Co^{2+} + 2e^- \rightarrow Co \tag{4.6}$$

occurs and thus cobalt is electrodeposited on the target substrate.

To promote plating uniformity, a highly conductive seed layer of gold was deposited prior to electrodeposition. The constants for cobalt required to estimate the plating rate are shown in Table 4.2.

MW_{Co}	58.9332 g/mol
ρ_{Co}	8.71 g/cm^3
ion	Co^{2+}

Table 4.2: Cobalt material constants [29].

Given the parameters in Table 4.1 and the cobalt constants in Table 4.2, the electrodeposition rate is approximately 7.02 $\frac{nm}{s}$.

4.2.3 Heterostructure Pill Soft Magnetic Layer

Nickel was electrodeposited through photoresist holes that corresponded to the shape of heterostructure pills. For nickel electrodeposition, a commercial solution and a soluble nickel anode from Technic Inc. [31] were used. The pre-made solution components are shown in Table 4.3.

Component
$Ni(SO_3NH_2)_2$
$NiBr_2$
H_3BO_3
proprietary wetter
proprietary additives

Table 4.3: Nickel sulfamate electroplating solution components (Technic Inc.).

Similar to cobalt electrodeposition, the setup of the nickel electrodeposition process is shown in Figure 4-3 along with the reactions occurring at the nickel electrode and target substrate as a voltage with specified polarity is applied.

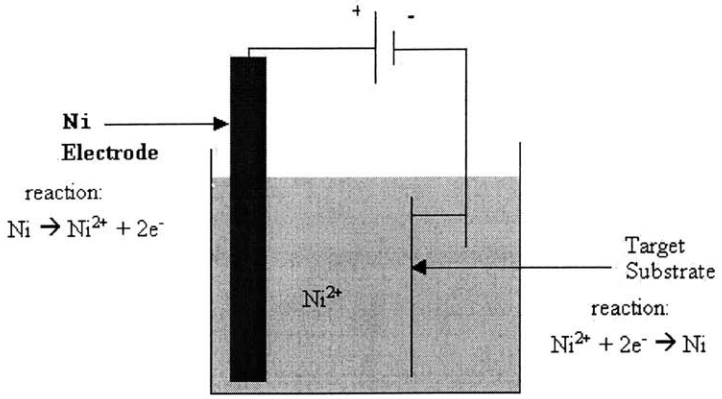

Figure 4-3: Nickel electrochemical cell denoting the reactions occurring at the anode and the cathode.

Material parameters for nickel are shown in Table 4.4

MW_{Ni}	58.69 g/mol
ρ_{Ni}	8.9 g/cm^3
ion	Ni^{2+}

Table 4.4: Nickel material constants [29]

Since the efficiency of this bath is near 100% and given the parameters in Tables 4.3 and 4.4, the nickel electrodeposition rate is estimated to be approximately 0.342 J $\frac{nm}{s}$, where J is the current density in units of $\frac{mA}{cm^2}$.

As the films are quite thin, it was difficult to realize good thickness uniformity across a sample substrate. Moreover, it was challenging to reduce the electrodeposition thickness variation from run-to-run. The thickness profile shown in Figure 4-4 shows the pill-to-

pill electrodeposition thickness variation encountered when looking at the plating thickness from the center of the substrate to the right toward the edge of the substrate. As can be seen, the plating occurs faster at the edge near the point of electrode electrical contact than at the center of the substrate. Depositing a conductive seed layer before electrodeposition improved uniformity and reduced run-to-run thickness variation, but requires two additional process steps, a metal deposition and a seed layer etch removal. Adding these steps reduces the benefits of electrodeposition with respect to the subtractive process.

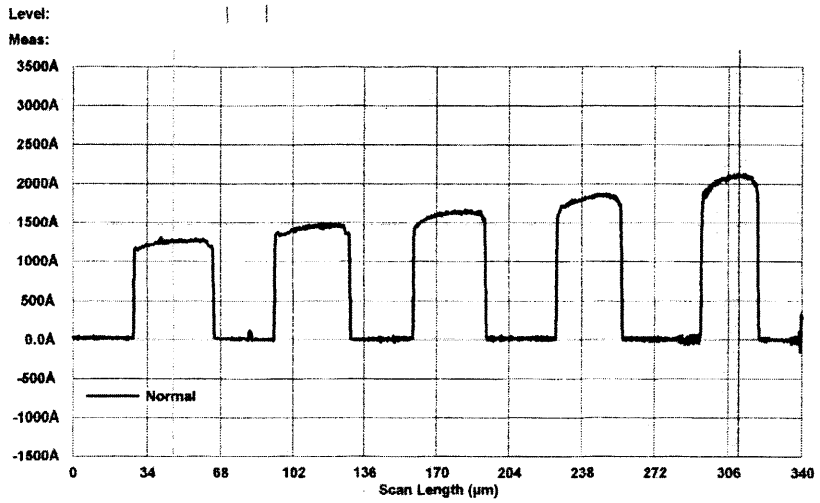

Figure 4-4: Profilometer measurement of electrodeposited nickel/gold/nickel/gold on p-type GaAs showing the level of uniformity between adjacent pill structures.

4.3 Magnetic Layer Definition – Subtractive Process

4.3.1 Physical Sputter Etching Background Theory

To circumvent this problem with reactive ion etching, physical sputter etching is one technique that was used to etch the magnetic film. Physical sputter etching as its name implies is strictly a physical process and involves no chemical etching. In a typical process, an argon ion plasma is generated in a low pressure chamber. An electric field is

applied which directs the ions toward the substrate surface. The ions accelerated by the electric field have enough energy to physically remove or "sputter" the magnetic material.

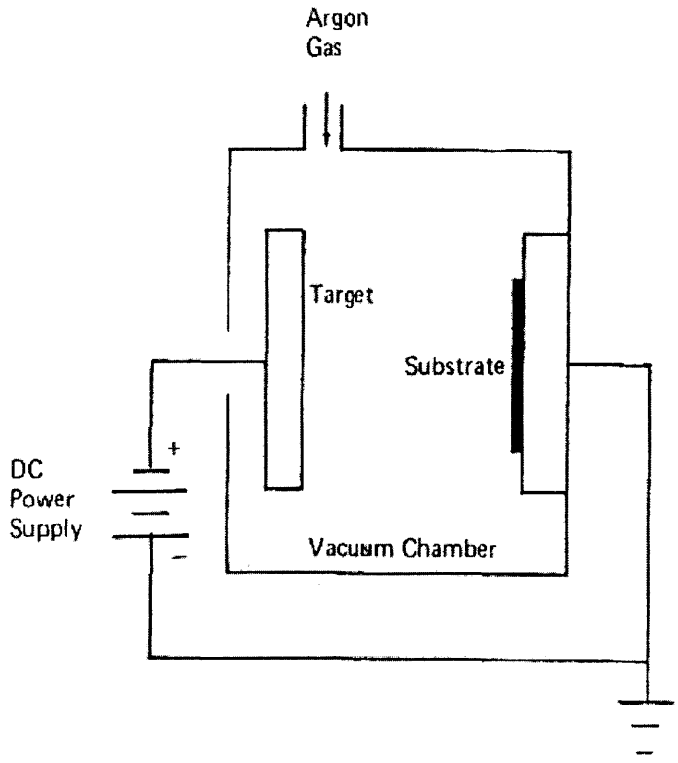

Figure 4-5: Physical sputter etching schematic [32].

Although physical sputter etching can result in very anisotropic etching, a few process compatibility issues must be taken into account when implementing this technique. First, since physical sputter etching is a mechanical process, other materials such as photoresist masks tend to be etched at the same rate or faster than the material designated for etching. Thus, very thick masks are required and the sidewall steepness of the etch can be limited.

Another issue with sputter etching is that since the ions are accelerated to high energies to bombard the material surface, substantial heating of the sample can occur. This is problematic for photoresist masks since they can become hardened to the point that they are virtually unremovable by standard stripping techniques such as solvent cleaning or

oxygen plasma ashing. Third, redeposition of material is also a concern with ion milling as it can result in micron scale etch masks that hinder uniform etching. Fortunately, in our research, the thickness of the layer sputter etched is relatively thin (around 0.3 um). Therefore, this redeposition and etch blocking is less problematic than if a long etch was required to etch a thick layer.

4.3.2 Target Substrate Hard Magnetic Layer

A 250 period thick Co (0.28 nm)/Pd (0.6 nm) multi-layer film was sputter deposited and patterned by a combination of e-beam lithography and ion milling into a two micron period of bars and spaces by Prof. T.C. Chong's group at the Data Storage Institute on the campus of the National University of Singapore.

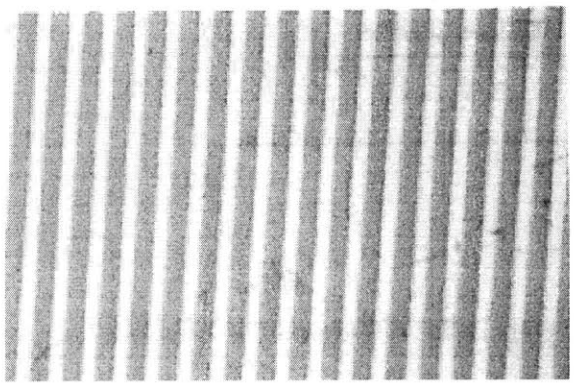

Figure 4-6: 250 period thick Co/Pd patterned bars having approximately a 2 micron lateral period.

From Atomic Force Microscope (AFM) imaging of the Co film, the grains are visible as is shown in Figure 4-7.

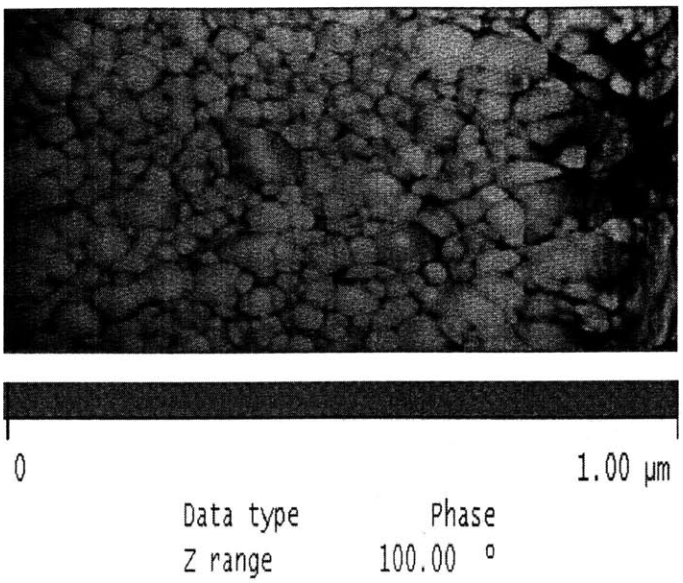

Figure 4-7: Atomic Force Microscope image of the cobalt grain size on the sample provided by Prof. T.C. Chong's group at the Data Storage Institute on the campus of the National University of Singapore.

4.3.3 Heterostructure Pill Soft Magnetic Layer

The subtractive process to generate patterned magnetic films corresponding to the device pills was carried out by the physical sputter etching process. The main problem involved with using physical sputter etching to pattern the nickel is that it renders the photoresist mask unremovable upon completion of the etch. An acetone rinse, a soaking in hot (85 °C) Microstrip 2001 for over an hour, as well as an oxygen plasma ashing for over two hours were tried to remove the photoresist. All efforts were unsuccessful. An image of the photoresist that has been hardened by bombarding it with argon ions is shown in Figure 4-8.

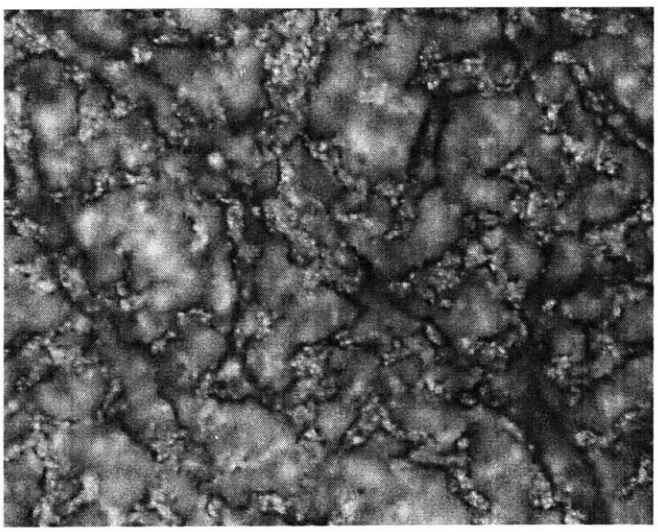

Figure 4-8: Photoresist following a 30 minute 125 W argon ion sputter etching.

With this resist unremovable, our attempts at performing the integration were hindered. Figure 4-9 shows an etched free pill assembled in an oversized recess with its nickel side up. Hardened photoresist is still covering the nickel.

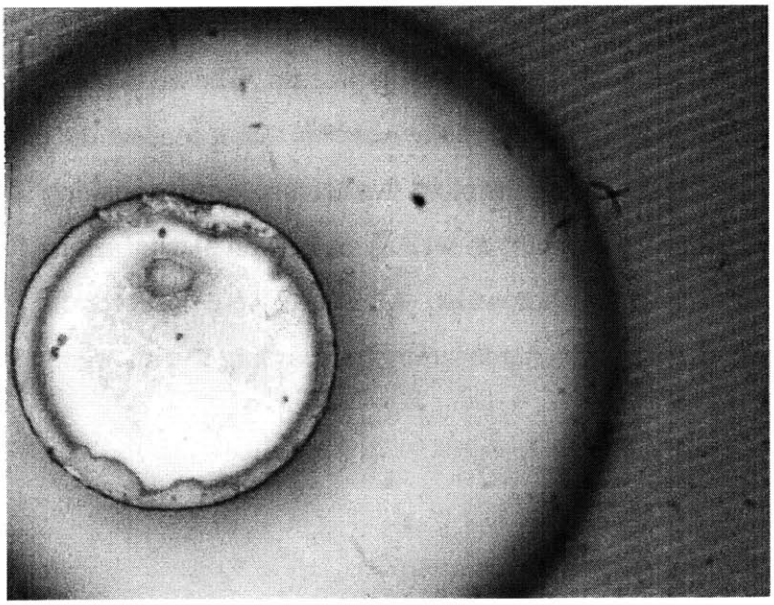

Figure 4-9: Oversized recess containing pill with nickel side up and with hardened photoresist still covering it.

Due to the difficulty removing the photoresist mask following sputter etching, a silicon dioxide, SiO_2, mask was used instead of a photoresist mask to protect the pills during the nickel sputter etch. To pattern the oxide mask, a photoresist mask was utilized. As is shown in Figure 4-10, the reactive ion etching process hardens the resist mask less than the sputter etching step and the resist was stripped completely in Microstrip 2001 solution.

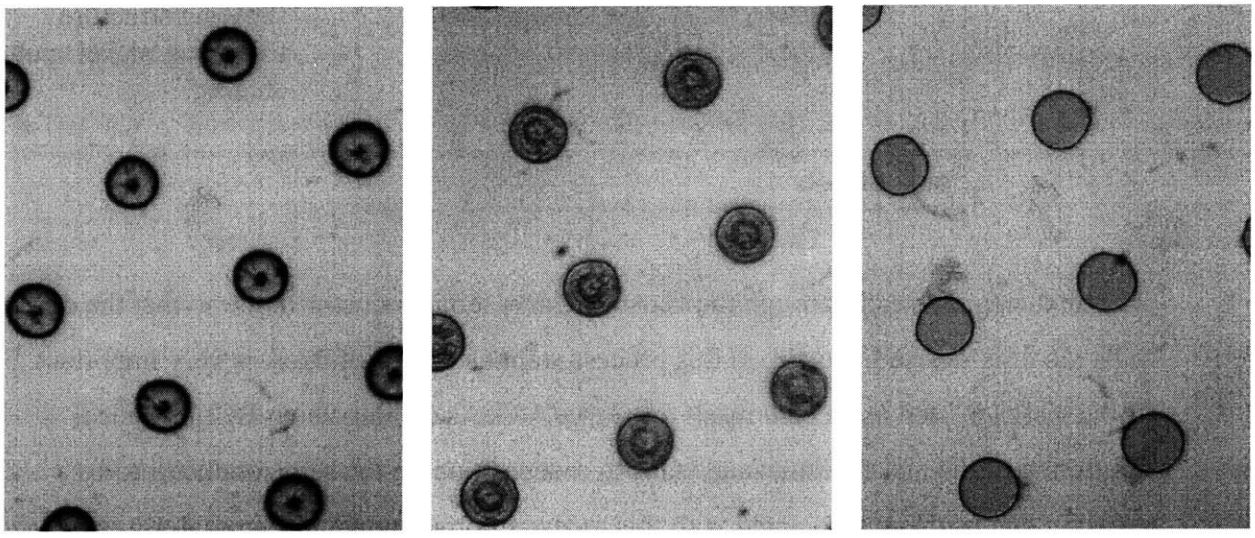

(a) (b) (c)

Figure 4-10: Photoresist removal procedure post SiO_2 reactive ion etching: (a) Image of photoresist pill masks following a 45 minute SiO_2 RIE using CF_4 gas, (b) Image of photoresist pill masks following a 2 minute acetone clean and solvent rinse, (c) Image of photoresist pill masks following an 80 minute 75° C Microstrip 2001 bath.

The 1 micron SiO_2 mask held up extremely well to both a 40 minute nickel sputter etch and a 90 minute GaAs/AlGaAs reactive ion etch

4.4 Heterostructure Pill Definition Beyond Magnetic Layer Patterning

4.4.1 Semiconductor Patterning

A schematic of the pill substrate following the patterning of the magnetic layer is shown in Figure 4-11.

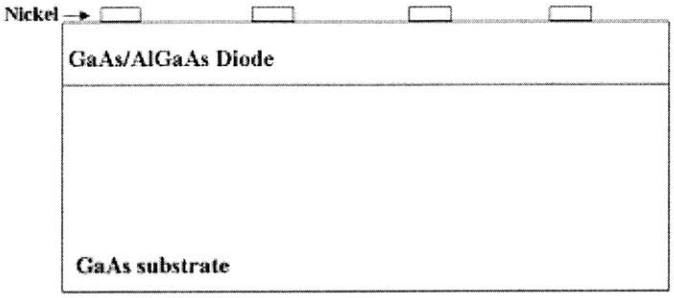

Figure 4-11: Schematic showing structure following nickel sputter etching.

The next step is to etch through the GaAs/AlGaAs semiconductor diode so that the device pills are fully defined. Again, in this process step the choice of mask is very important. If the nickel is used as an etch mask for GaAs/AlGaAs etching using BCl_3, physical sputtering of the nickel results and leads to redeposition on the semiconductor to be etched. The problem associated with this redeposition is shown in Figure 4-12, where nickel micromasks were formed during the GaAs/AlGaAs reactive ion etch.

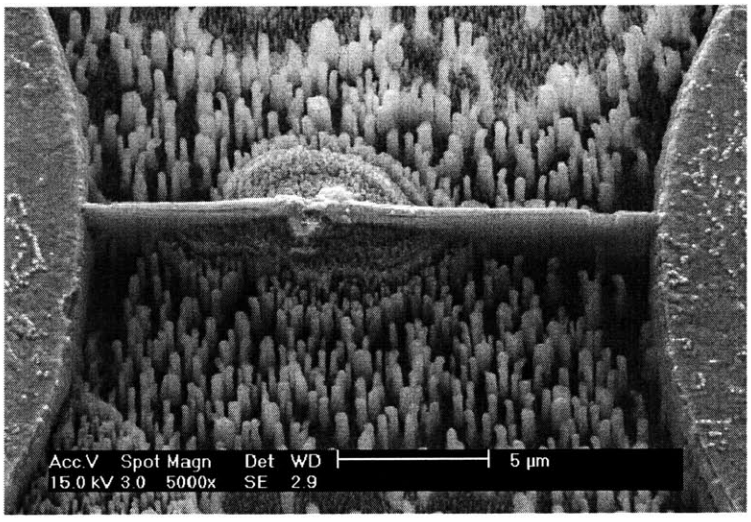

Figure 4-12: Redeposition micro-masking reactive ion etching resulting in grass structure.

Thus, two other mask materials, SiO_2 and photoresist, were used to protect the nickel during the GaAs/AlGaAs RIE. Both the 1 micron thick SiO_2 mask and the 6 micron thick photoresist mask held up well to this etching process. However, the photoresist mask provides better protection later on in the process during the pill undercut step and thus is the optimal choice at this point for masking the nickel during the GaAs/AlGaAs etch.

The GaAs/AlGaAs etching process consists of a four steps. Initially, the semiconductor is reactively ion etched at a rate of approximately 0.1 $\frac{um}{\text{min}}$ for 45 minutes using boron trichloride gas, BCl_3. Inspection of the sample following this dry etching reveals the formation of some etch residue shown in Figure 4-13.

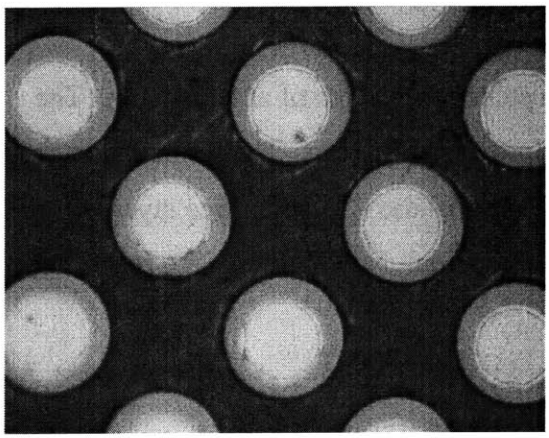

Figure 4-13: Heterostructure pill with surrounding etch residue following the 45 minute BCl_3 reactive ion etch.

To remove this residue, the sample is wet etched in a phosphoric acid, H_3PO_4, and hydrogen peroxide, H_2O_2, solution for roughly 90 seconds. This further etches the GaAs/AlGaAs and removes the residue as is shown in Figure 4-14.

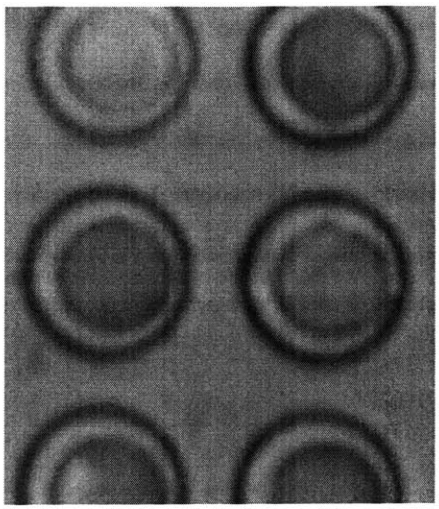

Figure 4-14: Heterostructure pill following the dilute phosphoric acid / hydrogen peroxide wet etch showing the removal of the etch residue.

The third step involves a second 45 minute reactive ion etching using BCl_3. Fourth, the sample undergoes a 1 minute phosphoric acid and hydrogen peroxide wet etch.

At this point, the area around the pills has been etched to a depth of at least 7 um. The pill height with nickel ferromagnetic layer is approximately 6 um. The semiconductor is etched well beyond the bottom of the pill, to ensure that the AlAs etch free layer will be fully exposed to the wet etchant during the undercut etch. Now, the pills are ready to be etched free from their substrate.

4.4.2 Final Preparation for Assembly

The heterostructure pills are etched free from their substrate using a selective wet chemical etch consisting of 25% hydrofluoric acid / 75% de-ionized water. Yablonovitch et al. reported over a 10^7 selectivity when etching free a 50 nm AlAs film using an $Al_{0.4}Ga_{0.6}As$ mask [33]. Even greater selectivity should be involved when considering AlAs and GaAs.

Unfortunately, although this etchant is very selective with relation to AlAs/GaAs, the ferromagnetic nickel layer is slowly eaten away by the etchant if it comes in contact with

it. Thus, a protective mask must be used to shield the nickel film from the chemical etchant. Thus, as was mentioned in the previous section, the photoresist mask provides better protection during this undercut process. This is due to the fact that the photoresist can be deposited on both the top and the sides of the nickel as is shown in Figure 4-15

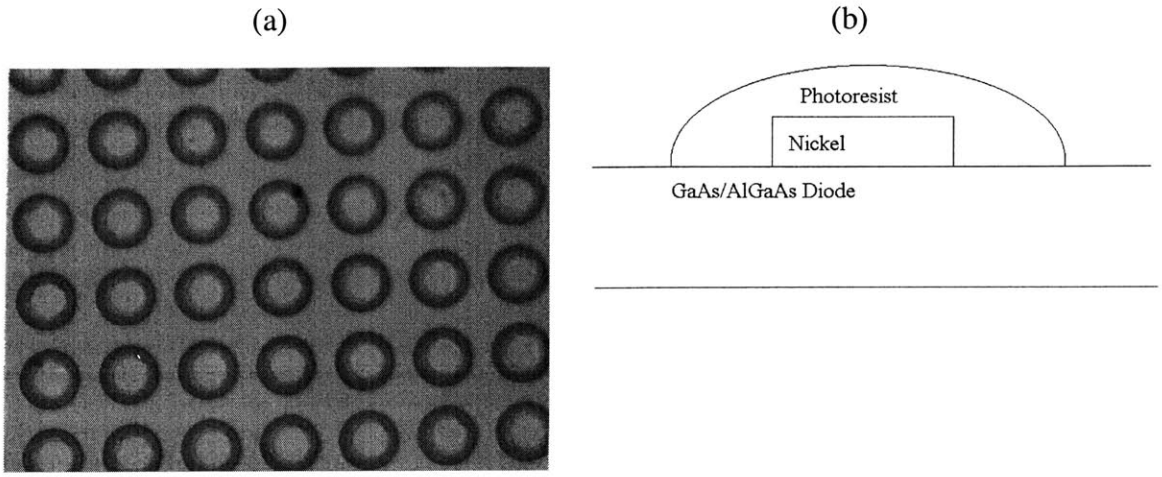

Figure 4-15: Photoresist masks were used to protect the nickel from the wet etchants: (a) Photograph of photoresist mask protecting the nickel where the inner light circles correspond to photoresist on top of nickel and the outer circles show the lateral extent of the photoresist masks, (b) Drawing of photoresist mask protecting the nickel.

Typically, the 100 nm thick, 45 um diameter AlAs pill layer is etched through in approximately 45 minutes and the pills are released from their native substrate as is shown in Figure 4-16.

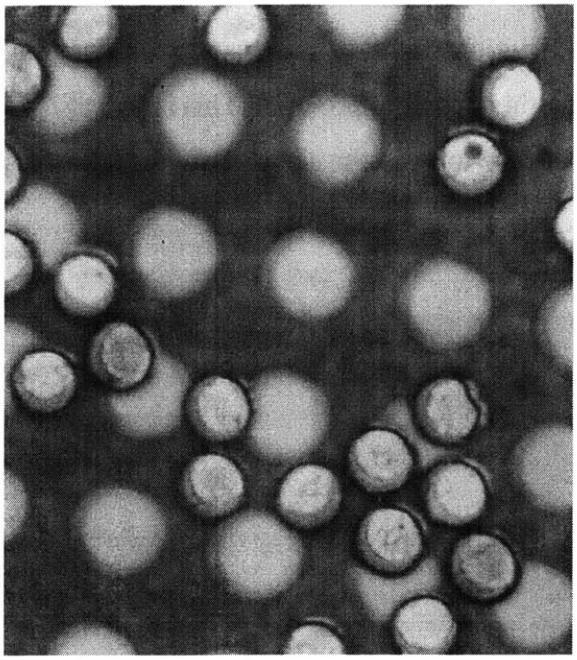

Figure 4-16: Following the undercut etch, many pills move along their host substrate where they congregate in bunches.

Following the process of the pills being etched free from their substrate, the pills lay freely on the substrate. A strip of adhesive is then used to remove the pills from the substrate. Following a couple of applications of this adhesive, most of the pills are transferred from the substrate to the adhesive as is shown in Figure 4-17. The adhesive is then inserted into a small vial (volume < 5 mL) of de-ionized water. This solution is then heated to a temperature of 140 °F at which point the adhesive dissolves and the pills are concentrated in a small volume of aqueous solution.

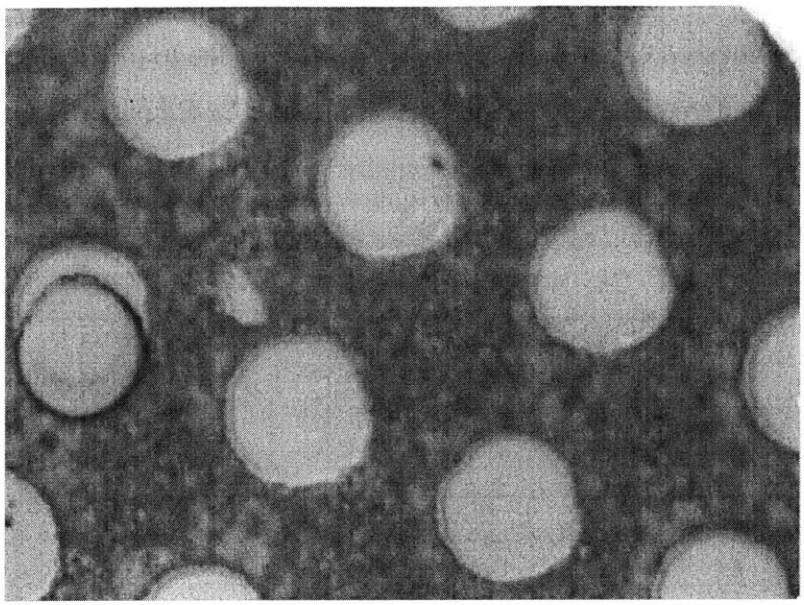

Figure 4-17: Picture showing that most pills are removed from their native substrate following adhesive removal.

4.5 Target Substrate Dielectric Recess Processing

To provide a location for the heterostructure pills to assemble, dielectric recesses with shape and size corresponding to the pills were formed on the host substrate. These silicon dioxide recesses were formed on the host substrate by first depositing SiO_2 using plasma enhanced chemical vapor deposition (PECVD). This process involves flowing silane (SiH_4) and nitrous oxide (N_2O). Nitrous oxide is used instead of oxygen since the use of pure oxygen tends to be too reactive and often produces lots of powder. This contamination often results in what is known as a showerhead pattern which corresponds to white circles having shape and size comparable to the dimensions of the gas inlets into the chamber. Focusing in on these large white circles, one sees that they correspond to a countless number of powder particles.

The reaction occurring during silicon dioxide growth is

$$SiH_4 + N_2O \rightarrow SiO_2 + 2N_2 + 2H_2 \qquad (4.7)$$

SiO_2 has been PECVD deposited successfully on both silicon and nickel substrates. Deposition on the patterned Co/Pd substrate proved difficult due to the topography associated with the pattern. The deposition conforms to the Co/Pd pattern as is shown in Figure 4-18

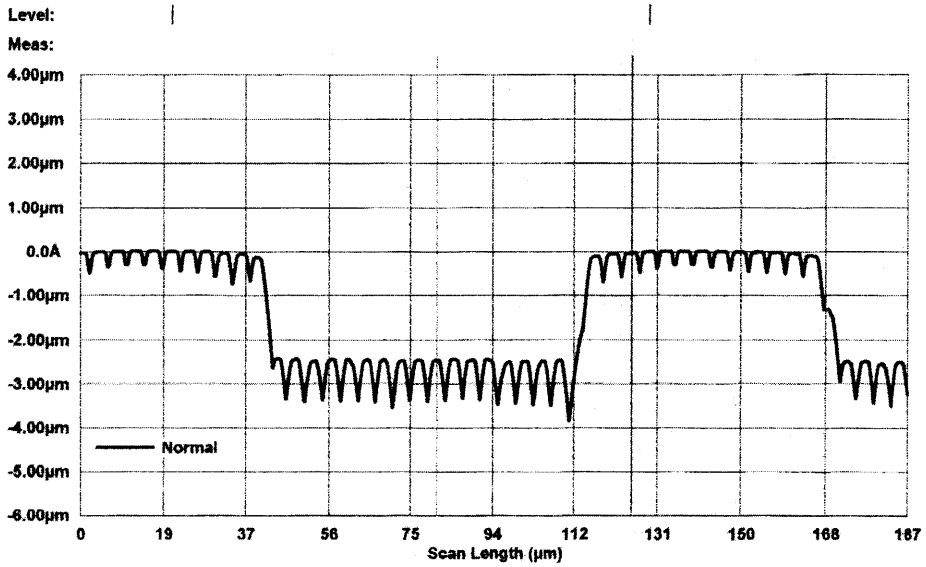

Figure 4-18: Profilometer measurement of a sample of SiO_2 deposited on top of the patterned Co/Pd with a recess etched in the SiO_2.

Recesses are reactively ion etched in the SiO_2 layer at a rate of approximately 33 $\frac{nm}{\text{min}}$ using freon, CF_4. The etching process involves a two-step process where the generation of the plasma in the RIE chamber results in the reaction

$$CF_4 \rightarrow CF_3^+ + F^- . \tag{4.8}$$

Fluorine free radicals, F^*, react with the SiO_2 through the following reaction resulting in the formation of the volatile compound SiF_4 [34].

$$SiO_2 + 4F^* \rightarrow SiF_4 + O_2 \tag{4.9}$$

This etch was also problematic for etching SiO_2 recesses on the patterned Co/Pd sample due to the topography. The main difficulty was determining the endpoint of the etch by visual inspection. Unfortunately, the SiO_2 was etched too long and part of the Co/Pd was physically etched away as is shown in Figure 4-19.

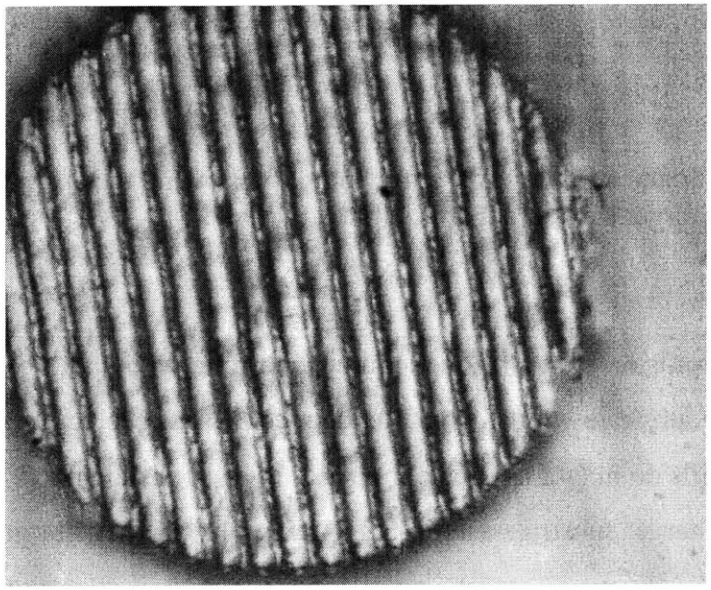

Figure 4-19: Photograph of a recess in SiO_2 that has been etched too long. Some of the Co/Pd patterned bars have been partially physically etched.

4.6 Assembly Results

The assembly process at this stage has involved the extraction of a solution of pills from a vial using a medicine dropper and the placement of the pills over an inclined target substrate as is shown in Figure 4-20.

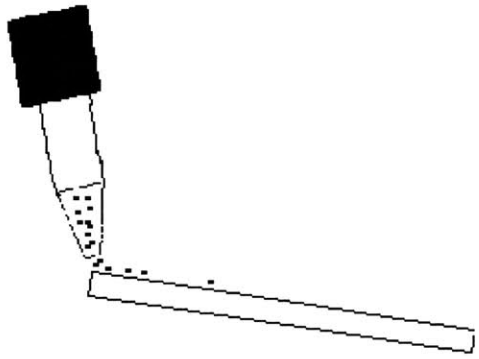

Figure 4-20: Schematic of the assembly process showing the dropping of a pill containing solution on a target substrate that is slightly inclined.

Assembly of pills on both a magnetic target substrate with photoresist recesses and a silicon target substrate with silicon dioxide recesses has been carried out. Some of the undersized pills do in fact assemble in the recesses as is shown in Figure 4-21 for the nonmagnetic target substrate and Figure 4-22 for the magnetic target substrate.

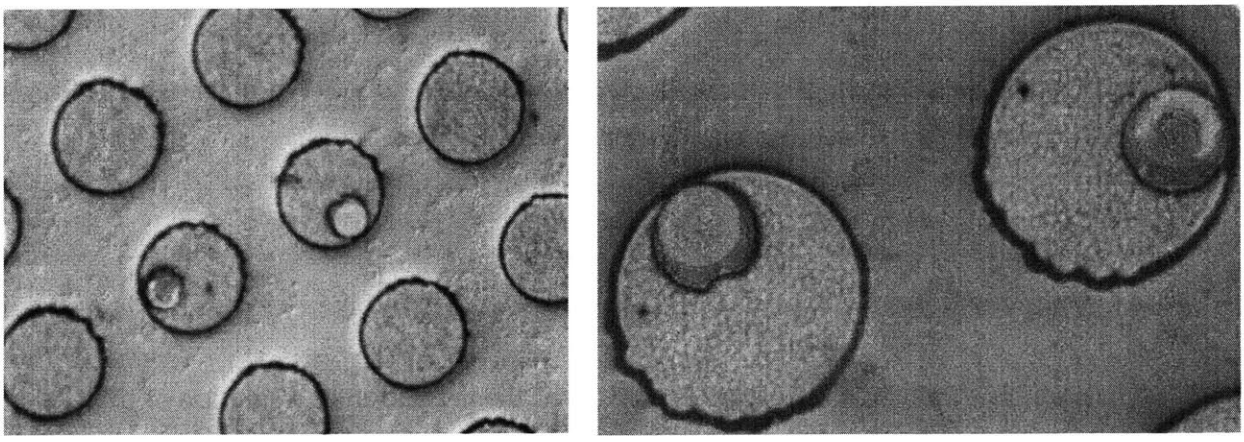

(a) (b)

Figure 4-21: Pills assembled in SiO_2 recesses on a non-magnetic silicon substrate: (a) Some pills assemble in the recess, but most recesses remain empty due to the small number of pills in comparison to the number of recesses, (b) Zoom in image of assembled pills.

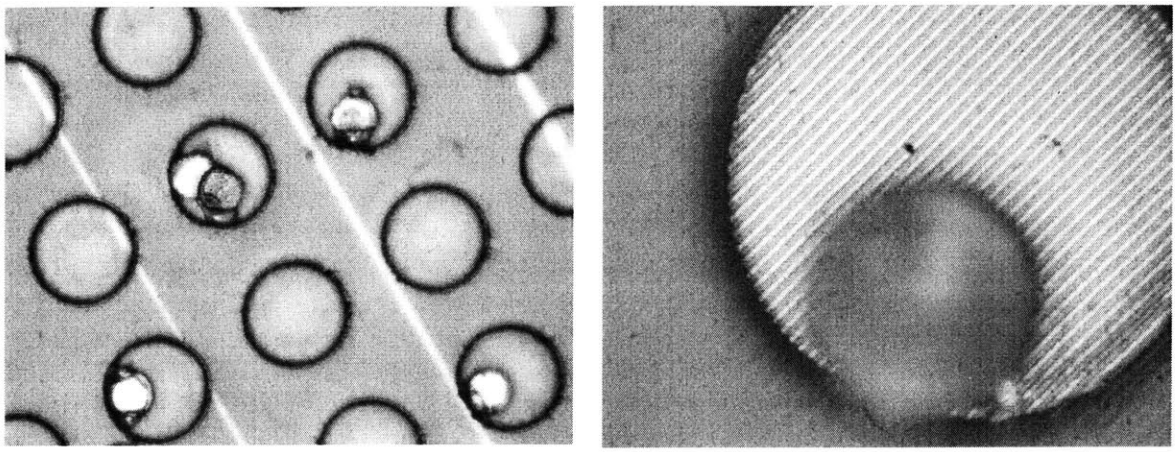

(a) (b)

Figure 4-22: Pills assembled in thick photoresist recesses on a magnetic Co/Pd multi-layer bar patterned on silicon substrate: (a) Pills assemble in some of the recesses with multiple pills assembling in one recess, (b) Zoom in of a pill assembled in a recess.

Unfortunately we have been unable to fabricate a large enough number of these pills to carry out a proper demonstration of the assembly. Thus, most of the recesses remain empty which makes it difficult to see the percentage of pills being retained by the substrate. The target substrates have been turned upside down following assembly. Many of the pills still remain in their recesses even on the non-magnetic target substrate, but a better understanding of the retention would be realized from an assembly where almost all recesses are filled with comparably sized pills.

Chapter 5

Conclusion and Future Work

Thus far, great strides have been made in the MASA process technology and in the magnetic characterization of the magnetic films. The magnetic layer deposition, semiconductor and magnetic layer patterning, and release etch of heterostructure diode pills with a nickel film have been successively carried out. The deposition and patterning of the soft nickel magnetic film has been accomplished using an additive process as well as a subtractive process with the magnetic characteristics of these films having been shown to be very similar.

In terms of possible future improvements, permalloy, $Ni_{79}Fe_{21}$, could be substituted for nickel. Permalloy is a softer magnetic material and should provide a better path for the magnetic flux created by the hard magnetic film since the out-of-plane field emanating from the hard magnetic layer should be sufficient to saturate a permalloy film; whereas, it may be too small to completely saturate the nickel film. To achieve better soft magnetic electrodeposit uniformity on the heterostructure pill substrate, a conductive seed layer could be used. This would reduce the resistive drop that occurs across the plating substrate and results in the pill-to-pill non-uniformity shown in Figure 4-4. If this technique was expanded to full wafer processing the conductive seed layer would be required.

The heterostructure diode pills GaAs/AlGaAs etching routine has been successfully implemented. A future improvement to this process will be to minimize the wet etching steps that follow the dry etching steps and are aimed at removing etch residue built up after the semiconductor reactive ion etching. This wet etch is isotropic and therefore intrudes laterally into the pill.

Regarding the target substrate, a Co/Pd multi-layer film was obtained from Prof. T.C. Chong's group at the Data Storage Institute on the campus of the National University of Singapore and characterized magnetically. This sample provides an optimal out-of-plane easy magnetization direction. An electrodeposited Co film has been fabricated in-house and characterized magnetically. This sample does not provide the desired out-of-plane magnetization. Thus, a future improvement will be to enhance the electrodeposited cobalt's out-of-plane magnetic characteristics by patterning the film so that the vertical dimension is the long dimension. This patterning should introduce an out-of-plane shape anisotropy that may be significant enough to reorient the magnetization out-of-plane.

SiO_2 recesses have been processed reliably on a silicon target wafer. The formation of SiO_2 recesses on the patterned Co/Pd sample has been problematic due to the sample topography. A potential solution may be to deposit and pattern the SiO_2 recesses prior to depositing the hard magnetic layer. This is possible if the hard magnetic layer is electrodeposited.

Much of the future work will be devoted to the assembly process. As was shown in Figures 4-21 and 4-22, the small size of the pills in comparison to the recesses and the small quantity of pills in relation to the number of recesses has made verification of the magnetic retentive force difficult. Thus, in terms of the assembly related future work, the pill size will be made more comparable to the size of a SiO_2 recess. Second, a much larger number of pills will be used in the assembly to determine the viability of filling a large density of recesses. Upon successful demonstration of the assembly under these conditions, other improvements such as a re-circulating fluid flow setup that would reflow the unassembled pills over the target substrate will be investigated.

Ultimately, following the implementation of the above improvements and the thorough demonstration of the MASA assembly technique, the integration of heterogeneous devices will be carried out.

Appendix A

Process Flows

Herein are contained the process flows utilized in the MASA process development. A more in-depth description of the process step recipes are given in Appendix B.

Table A.1 Heterostructure pill magnetic layer additive process.

Step	Description	Chemistry	Tool / Lab	Note
1000	Heterostrucure Growth	N/A	Fonstad MBE	Performed by Henry Choy
1010	Pill Recess S/E/D	N/A	EML	Resist = OCG-825, t = 1 um Exp = 4.5 s/um, Dev = 105s
1020	Ni electrodeposition	Technic Nickel 'S' Soln.	Fonstad Wet Bench	0.25 um thickness, T=38C

Table A.2 Heterostructure pill magnetic layer subtractive process.

Step	Description	Chemistry	Tool / Lab	Note
1000	Heterostrucure Growth	N/A	Fonstad MBE	Performed by Henry Choy
1010	Nickel Deposition	50 sccm Ar	EML/Sputter	t = 0.25 um
1020	SiO_2 Deposition	SiH_4, N_2O	EML/PECVD	t = 1 um
1030	SiO_2 Pill Cover S/E/D	N/A	EML/Photolithography	Resist: AZ4620, t = 6 um
1040	SiO_2 Etching	CF_4	EML/RIE	
1050	Resist Removal	Microstrip 2001	EML/Solvent Hood	time = 80 min, T = 75 C
1060	Ni Sputter Etching	50 sccm Ar	EML/Sputter	

Table A.3 Heterostructure pill semiconductor etch through release etch process.

Step	Description	Chemistry	Tool / Lab	Note
1100	Start with patterned nickel on diode substrate	N/A	N/A	N/A
1110	Pill Cover S/E/D		EML/Photolithography	Resist: AZ4260, t = 6 um
1120	GaAs/AlGaAs Dry Etch	12 sccm BCl_3	EML/RIE	45 minutes
1130	GaAs/AlGaAs Wet Etch	10:1:1 DI:H_2O_2(30%): H_3PO_4(85%)	Fonstad Wet Bench	90 seconds
1140	GaAs/AlGaAs Dry Etch	12 sccm BCl_3	EML/RIE	45 minutes
1150	GaAs/AlGaAs Wet Etch	10:1:1 DI:H_2O_2(30%): H_3PO_4(85%)	Fonstad Wet Bench	60 seconds
1160	AlAs Etch	25% HF: 75% H_2O	Fonstad Wet Bench	< 60 minutes
1170	Resist Removal	O_2 plasma	EML/Asher	60 minutes

Table A.4 Target wafer magnetic layer additive process.

Step	Description	Chemistry	Lab / Tool	Note
1000	Sample Degrease	Acetone, Meth, IPA	EML/Solvent Hood	N_2 dry
1010	Native Oxide Removal	BOE	EML/Acid Hood	10-20 second dip, H_2O rinse, N_2 dry
1020	Electroplating Seed deposition	Cr/Au	EML Sputter	
1030	Co Electrodeposition	N/A	Fonstad/Chemical Hood	

Table A.5 Target wafer subtractive process including magnetic layer definition and SiO_2 recess formation.

Step	Description	Chemistry	Lab / Tool	Note
1000	Sample Degrease	Acetone, Meth, IPA	EML/Solvent Hood	N_2 dry
1010	Native Oxide Removal	BOE	EML/Acid Hood	10-20 second dip, H_2O rinse, N_2 dry
1020	Pd(0.28 nm) / Co(0.6 nm) Deposition	N/A	Singapore	250 multilayers. Performed by Chong (Singapore)
1030	Magnetic Stripe S/E/D	N/A	Singapore	Performed by Chong (Singapore)
1040	Magnetic Stripe Ion Milling	N/A	Singapore	Performed by Chong (Singapore)
1050	Wafer Clean	Acetone, Meth, IPA	EML/Solvent Hood	
1060	SiO_2 Deposition	SiH_4, N_2O	EML/PECVD	
1070	Recess S/E/D	N/A	EML/Contact Aligner	Resist: AZ4620, t = 6 um
1080	SiO_2 Etch	CF_4	EML/RIE	

Appendix B

Process Recipes

B.1 Lithography Processing Recipes

The following recipes are expanded descriptions of the lithography Spin/Expose/Develop (S/E/D) process steps listed in Tables A.1 through A.5. All masks used in the following lithography process recipes were made by James Perkins, a fellow student in Professor Fonstad's research group with whom I collaborated with closely on the MASA project.

B.1.1 Pill Recess S/E/D (Standard Positive Photoresist (OCG-825)) Lithography

The Pill Recess S/E/D lithography process step was used to pattern 1 um photoresist holes prior to the nickel electrodeposition and corresponds to process step 1010 in Table A.1.

1.) Solvent Clean (Acetone, Methanol, IPA, N_2 Blow Dry)
2.) Prebake (200 °C) 20 minutes
3.) HMDS static dispense
    a. 30 seconds at 4000 rpm
4.) Bake (130 °C) 10 minutes
5.) PR Dynamic dispense (OCG-825)
    a. 5 seconds at 750 rpm
    b. 30 seconds at 3000 rpm
6.) Softbake (90 °C) 30 minutes
7.) Exposure (Karl Suss MJB3 Contact Aligner) 4.5 seconds
8.) Develop (934 1:1) 105 seconds

9.) Postbake (120 °C) 30 minutes

B.1.2 SiO_2 Pill Cover S/E/D and Pill Cover S/E/D (Thick Photoresist (AZ4620)) Lithography

This lithography process step was used to pattern 6 um photoresist pill covers prior to the SiO_2 mask etching step in Table A.2 and 6 um photoresist pill covers prior to the GaAs/AlGaAs reactive ion etch in Table A.3. This lithography recipe is used in process step 1030 in Table A.2 and process step 1110 in Table A.3.

1.) Solvent Clean (Acetone, Methanol, IPA, N_2 Blow Dry)
2.) Prebake (200 °C) 20 minutes
3.) HMDS static dispense
    a. 30 seconds at 4000 rpm
4.) Bake (130 °C) 10 minutes
5.) PR Dynamic dispense (AZ4620)
    a. 10 seconds at 1500 rpm
    b. 60 seconds at 3000 rpm
    c. 10 seconds at 5000 rpm
6.) Softbake (90 °C) 60 minutes
7.) Exposure (Karl Suss MJB3 Contact Aligner) 24 seconds
8.) Develop (AZ440) 150 seconds
9.) Hardbake (90 °C) 30 minutes

B.1.3 Image Reversal Photoresist (AZ5214E) Lithography

This lithography process step was used at times to pattern photoresist recesses and photoresist pill covers. None of the process steps in Tables A.1 through A.5 utilize this recipe though.

1.) Solvent Clean (Acetone, Methanol, IPA, N_2 Blow Dry)
2.) Prebake (200 °C) 20 minutes
3.) HMDS static dispense
    a. 30 seconds at 4000 rpm
4.) Bake (130 °C) 10 minutes
5.) PR Dynamic dispense (AZ5214E)

a. 30 seconds at 2000 rpm

6.) Softbake (90 °C) 30 minutes
7.) Exposure (Karl Suss MJB3 Contact Aligner) 14 seconds
8.) Hardbake (105 °C) Hotplate 52 seconds
9.) Flood Exposure (Karl Suss MJB3 Contact Aligner) 2.7 minutes
10.) Develop (AZ422) 60 seconds

B.2 Deposition Process Recipes

The following recipes were used to deposit the materials used in the MASA technique and relate to the deposition process steps listed in Tables A.1 through A.5.

B.2.1 Nickel

A. Sputter Deposition

Machine: Materials Research Corp. 8620 Sputtering System
Gas Flow: 50 sccm Argon
Pumpdown Pressure: 1.0 x 10^{-6} torr
Pressure at Deposition: 8 mtorr
Power: 350 W
Deposition Rate: 14 nm/min

B. Electrodeposition

Solution: Technic Inc. Nickel "S" solution
Anode: Nickel
Current Density: ~ 74.3 mA/cm^2
Temperature: 38 °C
Deposition Rate: 0.342 J $\frac{nm}{s}$, where J is the current density in $\frac{mA}{cm^2}$.

2.) Gold

A. Sputter Deposition

Machine: Materials Research Corp. 8620 Sputtering System
Gas Flow: 50 sccm Argon
Pumpdown Pressure: 1.0 x 10^{-6} torr
Pressure at Deposition: 8 mtorr
Power: 200 W
Deposition Rate: 25 nm/min

B. Electrodeposition

Solution: Technic Techni-Gold 25 E
Anode: Platinum Clad
Current Density: 19.4 mA/cm^2
Temperature: 60 °C
Deposition Rate: 20.5 nm/s

3.) SiO_2

A. PECVD

Machine: Plasma-Therm Waf'r Batch 700D
Gas Flow: 280 sccm SiH4
800 sccm N2O
Pressure: 700 mtorr
Temperature: 300 °C
Power: 25 W
Deposition Rate: 50 nm/min

B. Sputter

Machine: Materials Research Corp. 8620 Sputtering System
Gas Flow: 20 sccm Argon
Pumpdown Pressure: 1.5 x 10^{-6} torr
Pressure at Deposition: 8 mtorr
Power: 300 W
Deposition Rate: 2.5 nm/min

4.) Cobalt

A. Electrodeposition

Solution: $CoCl_2 \cdot 6H_2O$ – 375 g/l
H_3BO_3 – 37.5 g/l
pH - 3.6
Anode: Cobalt
Current Density: 20 mA/cm^2
Temperature: room temperature
Deposition Rate: 7.02 $\frac{nm}{s}$.

B.3 Etching Process Recipes

The following recipes were used to etch the materials used in the MASA technique and relate to the etching process steps listed in Tables A.1 through A.5.

1.) GaAs/AlGaAs

A. Reactive Ion Etching

Machine: Plasma-Therm Waf'r Batch 700D
Gas Flow: 12 sccm BCl_3
Pressure: 10 mtorr
Power: 250 W INCP (Inductively Coupled Plasma)
Etch rate: ~ 0.08 um/min – 0.1 um/min

B. Wet etching

Solution:10:1:1 H_2O: H_2O_2 (30%): H_3PO_4 (85%)
Temperature: 25 °C
Agitation: 400 rpm (magnetic stirrer)
Etch Rate: 0.4 um/min

2.) SiO_2

A. RIE

Machine: Plasma-Therm Waf'r Batch 700
Gas Flow: 20 sccm CF_4
Pressure: 25 mtorr
Power: 300 W
Etch Rate: 2 um/hour

B. Wet etching

Solution: Buffered Oxide Etch (7 NH_4F: 1 HF)
Temperature: 25 °C
Agitation: No
Etch rate: ~1 um/min

3.) Nickel

A. Ion milling

Machine: Materials Research Corp. 8620 Sputtering System

Gas Flow: 50 sccm Argon
Pumpdown Pressure: < 2.5 x 10^{-6} torr
Pressure at Deposition: 8 mtorr
Power: 150 W
Etch Rate: > 12.5 nm/min

B. Wet etching

Solution: Transene Nickel Etchant Type TFB
Temperature: 25 °C
Agitation: 400 rpm (magnetic stirrer)
Etch rate: 30 Å/s
Notes: Does not attack gold films

4.) Gold

A. Wet etching

Solution: Transene Gold Etchant GE-8148
Temperature: 25 °C
Agitation: No
Etch rate: ~ 5 nm/s
Notes: Does not attack nickel films

Bibliography

[1] Y.K. Chen, et al., "Applications of Compound Semiconductors in High Data Rate Optical Fiber Communications," Proc. of the International Conference on Compound Semiconductor Manufacturing Technology. 2001.

[2] Bahaa E.A. Saleh and Malvin Carl Teich. Fundamentals of Photonics. pp. 633. John Wiley & Sons, Inc. 1991.

[3] S.M. Sze. Physics of Semiconductor Devices. pp. 751. John Wiley & Sons, Inc. 1981.

[4] A.R. Mickelson, N.R. Basavanhally, and Y-C Lee. Optoelectronic Packaging. John Wiley & Sons, Inc. 1997.

[5] Clifton G. Fonstad, "Very Large Scale Monolithic Heterogeneous Optoelectronic Integration: the Epitaxy-on-Electronics, Silicon-on-Gallium Arsenide, and Aligned Pillar Bonding Techniques" in Heterogeneous Integration: Proceedings of a Conference held January 25-26, 2000 in San Jose, CA edited by Elias Towe (Critical Reviews of Optical Engineering, Vol. CR76, SPIE Optical Engineering Press, Bellingham, WA 2000) Chapter 1.

[6] S.M. Sze. Physics of Semiconductor Devices. pp. 848-851. John Wiley & Sons, Inc. 1981.

[7] J.A. Carlin, M.K. Hudait, S.A. Ringel, D.M. Wilt, E.B. Clark, C.W. Leitz, M. Currie, T. Langdo, and E.A. Fitzgerald, "High Efficiency GaAs-on-Si Solar Cells with High V_{OC} Using Graded GeSi Buffers," Proc. IEEE Photovoltaic Specialists Conference, pp. 1006-1011, Sept. 2000.

[8] Motorola, Inc. website, http://www.motorola.com/mot/documents/0,1028,419,00.pdf.

[9] Hsi-Jen J. Yeh and John S. Smith, "Fluidic Self-Assembly of Microstructures and its Application to the Integration of GaAs on Si," Proc. IEEE MEMS-94 Workshop, pp. 279-284, Jan. 1994.

[10] John S. Smith, "High density, low parasitic direct integration by Fluidic Self Assembly (FSA)," Proc. IEEE Electron Devices Meeting, pp. 201-204, Dec. 2000.

[11] C.D. Nordquist, Peter A. Smith, and Theresa S. Mayer, "An Electro-fluidic Assembly Technique for Integration of III-V Devices onto Silicon," Proc. IEEE International Symposium on Compound Semiconductors, pp. 137-142, Oct. 2000.

[12] C.F. Edman, R.B. Swint, C. Gurtner, R.E. Formosa, S.D. Roh, K.E. Lee, P.D. Swanson, D.E. Ackley, J.J Coleman, and M.J. Heller. "Electric Field Directed Assembly of an InGaAs LED onto Silicon Circuitry," IEEE Photonics Tech. Letters, vol. 12, no. 9, September 2000.

[13] Clifton G. Fonstad, "Magnetically Assisted Statistical Assembly – a new heterogeneous integration technique," Singapore-MIT Alliance Symposium. January 2002.

[14] Richard M. Bozorth. Ferromagnetism. pp. IEEE Press. 1978.

[15] Robert C. O'Handley. Modern Magnetic Materials, Principles and Applications, pp. 43-47, 229-234, 619-642. John Wiley & Sons, Inc. 2000.

[16] H.J.G. Draaisma, F.J.A. den Broeder, and W.J.M. de Jonge, "Perpendicular Anisotropy in Pd/Co multilayers," J. Appl. Physics 63 (8), 15 April 1988.

[17] Digital Measurement Systems website, www.dms-magnetics.com/pdfpass/vsmmost.pdf.

[18] Digital Instruments, Inc. website, www.di.com/appnotes/mfm/mfmlift.html.

[19] M. Prutton. Thin Ferromagnetic Films. pp. 79-82. Butterworth Inc. 1964.

[20] P.F. Carcia, A.D. Meinhaldt, and A. Suna, "Perpendicular magnetic anisotropy in Pd/Co thin film layered structures," Appl. Phys. Lett. 47 (2), 15 July 1985.

[21] Kazuhiro Ouchi, "Recent Advancements in Perpendicular Magnetic Recording," IEEE Trans. on Magnetics, Vol. 37, no. 4, July 2001.

[22] J. Moritz et al., "Patterned Media made from Pre-etched wafers: A promising route toward Ultrahigh-density magnetic recording," IEEE Trans. on Magnetics, vol. 38, no. 4, July 2002.

[23] Brad N. Engel, Craig D. England, Robert A. Van Leeuwen, Michael H. Wiedmann, and Charles M. Falco, "Interface Magnetic Anisotropy in Epitaxial Superlattices," Physics Review Letters, vol. 67, no. 14, 30 September 1991.

[24] Brad N. Engel, Craig D. England, Robert A. Van Leeuwen, Masafumi Nakada, and Charles M. Falco, "Magnetic Properties of epitaxial Co/Pd superlattices," J. Appl. Phys. 69 (8), 15 April 1991.

[25] R. Hsiao, "Fabrication of Magnetic Recording Heads and Dry Etching of Head Materials," IBM Journal of R&D, vol. 43, ½, 1999.

[26] James Perkins, "Magnetically Assisted Statistical Assembly of III-V Heterostructures on Silicon: Initial Process and Technology Development," S.M. thesis, Massachusetts Institute of Techology Department of Electrical Engineering and Computer Science, May 2002.

[27] S.H Liao, "Electrodeposition of Magnetic Materials for thin-film heads," IEEE Trans. on Magnetics, vol. 26, no. 1, January 1990.

[28] C.N. Ting, D. Papapanayioton, Zhu Mei, "Electro-chemical deposition technology for ULSI multilevel copper interconnects," Proc. of the IEEE 5th International Conference on Solid-State and Integrated Circuit Technology, 1998.

[29] Mordechay Schlesinger and Milan Paunovic. Modern Electroplating, Fourth Edition. John Wiley & Sons, Inc. 2000.

[30] N.V. Myung, D.Y. Park, M. Schwartz, K. Nobe, H. Yang, C.-K. Yang, and J.W. Judy. Electrodeposited Hard Magnetic Thin Films for MEMS Applications. Sixth International Symposium on Magnetic Materials, Processes, and Devices, Proc. Electrochemistry Society. PV 2000-29. 2000.

[31] Technic Inc. Techni Nickel "S" (Nickel Sulfamate) electroplating solution technical data..

[32] Klaus K. Schuegraf. Handbook of Thin-film Deposition Processes and Techniques. pp.297. Noyes Publications. 1988.

[33] Eli Yablonovitch, T. Gmitter, J.P. Harbison, and R. Bhat. Extreme selectivity in the lift-off of epitaxial GaAs films, Appl. Phys. Lett. 51 (26), 28 December 1987.

[34] James D. Plummer, Michael D. Deal, Peter B. Griffin. Silicon VLSI Technology: Fundamentals, Practice, and Modeling. Prentice Hall. 2000.